

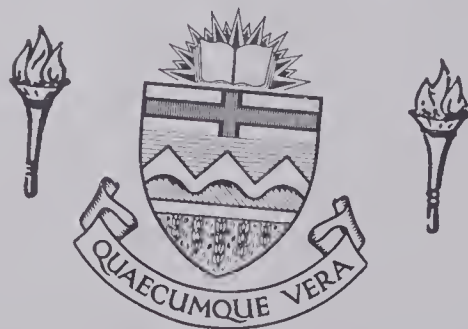
For Reference

NOT TO BE TAKEN FROM THIS ROOM

For Reference

NOT TO BE TAKEN FROM THIS ROOM

Ex libris
UNIVERSITATIS
ALBERTAENSIS



THE UNIVERSITY OF ALBERTA

ELECTRONIC ADMITTANCE OF
AVALANCHE DIODE OSCILLATORS

by



Muhammad Jamil Ahmed

A THESIS

SUBMITTED TO THE FACULTY OF GRADUATE STUDIES
IN PARTIAL FULFILMENT OF THE REQUIREMENTS FOR THE DEGREE
OF MASTER OF SCIENCE

DEPARTMENT OF ELECTRICAL ENGINEERING

EDMONTON, ALBERTA

SPRING, 1970

Thesis
1970
2

UNIVERSITY OF ALBERTA
FACULTY OF GRADUATE STUDIES

The undersigned certify that they have read, and recommend to the Faculty of Graduate Studies for acceptance, a thesis entitled ELECTRONIC ADMITTANCE OF AVALANCHE DIODE OSCILLATORS submitted by Muhammad Jamil Ahmed in partial fulfilment of the requirements for the degree of Master of Science.

Date. 23 December / '69

ABSTRACT

The electronic admittance of an avalanche diode oscillator, operating under steady-state conditions, has been investigated experimentally. The cw output power and frequency behaviour of the oscillator have been studied as functions of load impedance and of bias current. In order to gain insight concerning the behaviour of the diode at the onset of oscillations, the small-signal electronic admittance has been obtained as a function of bias voltage, for voltages less than the threshold voltage. Plots of the oscillator admittance show that, for low voltages, the circuit surrounding the diode dominates oscillator behaviour, while for increasing voltages the diode behaviour becomes increasingly dominant. The effect of load on the behaviour was studied by plotting the Rieke diagram. Discontinuous changes in oscillator signal frequency were observed with load variation and bias current variation; the discontinuous frequency changes were not reversible i.e., hysteresis characteristics were observed. The constant frequency curves of the Rieke diagram are skew, indicating that the electronic susceptance is a function of power level. The electronic admittance, with the oscillator in steady-state operation, was computed by using the data from the Rieke diagram.

ACKNOWLEDGEMENTS

I wish to thank my supervisor Dr. P. A. Goud for the support and encouragement during the course of this study; particularly at the times when nothing seemed to work. I am especially indebted to him for applying "mid-course corrections", as it is very easy to get side-tracked in research work.

Thanks are in order for Mr. James Fearn for maintenance of the equipment and help in the laboratory.

The financial assistance of the National Research Council of Canada and the University of Alberta are gratefully acknowledged. I feel that assisting in the demonstration of various experiments in undergraduate laboratories have helped me in my work.

TABLE OF CONTENTS

	Page
CHAPTER I: INTRODUCTION	1
CHAPTER II: THE OSCILLATOR CAVITY AND ITS OUTPUT-COUPLER SYSTEM	6
2.1 The Microwave Resonator and its Parameters	6
2.2 Determination of Equivalent Resonator Capacitance and Inductance	11
2.3 Procedure for the Evaluation of the Coupling-System Parameters	13
CHAPTER III: EXPERIMENTAL DETERMINATION OF THE OSCILLATOR EQUIVALENT CIRCUIT AND THE ELECTRONIC ADMITTANCE	21
3.1 Measurement of Resonator Capacitance	21
3.2 Measurement of Q_0	27
3.3 Procedure to Compute Electronic Admittance Below the Threshold Voltage	37
CHAPTER IV: RIEKE DIAGRAMS	41
4.1 The Oscillator Circuit	41
4.2 Properties of a Self-Excited Oscillator as a Function of Load	43
CHAPTER V: REFLECTOMETER BRIDGE SET-UP, DETERMINATION OF RIEKE DIAGRAM AND OF ELECTRONIC ADMITTANCE	52
5.1 The Reflectometer Bridge	52
5.2 Measurement Circuit Used	58
5.3 Calibration and Testing of Reflectometer Bridge	59

Chapter V, continued

5.4	Rieke Diagram and Circuit Admittance Measurements	62
5.5	Calculation of Electronic Admittance	65
5.6	Hysteresis Phenomena	67
5.7	Sources of Error	76
CHAPTER VI: CONCLUSIONS		79
REFERENCES		82
APPENDIX A		84

LIST OF TABLES

	Page
TABLE 3.1: Change of Diode Capacitance and of Circuit Resonant Frequency with Bias Voltage	26

LIST OF FIGURES

	Page
FIGURE 1. 1: Cross-Sectional Sketch of Avalanche Diode Oscillator	3
FIGURE 1. 2: Impurity Concentration Profile of Silicon Avalanche Diode	4
FIGURE 2. 1: Equivalent Circuit Representation of a Microwave Oscillator	8
FIGURE 2. 2: Simplified Equivalent Circuit of a Microwave Oscillator Designed to Operate in a Single Mode	9
FIGURE 2. 3: Equivalent Circuit of a Microwave Oscillator in "Cold" State	9
FIGURE 2. 4: Equivalent Circuit for the Avalanche Diode Oscillator of Fig. 2.3: The Transformer in Fig. 2.3 Replaced by an Ideal Transformer and a Series Secondary Inductance L_2	14
FIGURE 2. 5: Equivalent Circuit of an Avalanche Diode Oscillator	15
FIGURE 2. 6: Input Impedance of Resonator (a) The Input Impedance Referred to Plane a-a Near Resonant Cavity	17
(b) The Impedance Locus Referred to the Detuned Short Position	17
FIGURE 3. 1: Experimental Set-Up for Measuring the Change in Capacitance of ADO with Bias Voltage	22
FIGURE 3. 2: Change of Diode Capacitance and of Circuit Resonant Frequency with Bias Voltage	24
FIGURE 3. 3: Circuit Used for Cold-Tests on Avalanche Diode Oscillator	25
FIGURE 3. 4: Parallel and Series Equivalent Representation of a Resonant Cavity (a) The Equivalent Impedance Referred to the Plane of Detuned Short with Accompanying Impedance Plane Plot	28

Figure 3. 4, continued

(b) The Equivalent Impedance Referred to the Plane of Detuned Open with Accompanying Impedance Plane Plot	28
FIGURE 3. 5: (a) Variation in Position of Minimum Around Resonant Frequency	30
(b) Variation in Position of Minimum Around Resonant Frequency for an Undercoupled Cavity	31
FIGURE 3. 6: Variation in VSWR Around Resonant Frequency of Cavity	32
FIGURE 3. 7: VSWR vs Frequency for Different Bias Voltages	34
FIGURE 3. 8: Resonant Frequency vs Bias Voltage	35
FIGURE 3. 9: Circuit Admittance for Two Bias Voltages	36
FIGURE 3.10: Transformation of Z_{tot}	38
FIGURE 3.11: Small-Signal Electronic Admittance Y_{e1} vs Bias Voltage ($V < V_B$)	40
FIGURE 4. 1: Simplified Equivalent Circuit of Oscillator	42
FIGURE 4. 2: Ideal Rieke Diagram in B - G Plane	46
FIGURE 4. 3: Ideal Rieke Diagram in Circle-Diagram Form for the Same Oscillator as in Fig. 4.2	49
FIGURE 4. 4: Actual Rieke Diagram	51
FIGURE 5. 1: Reflectometer Bridge Set-Up for Determining the Effect of Load Admittance on Oscillator Behaviour	53
FIGURE 5. 2: The Microwave Reflectometer	55
FIGURE 5. 3: Reflectometer Arrangement with Hybrid-Ring	57
FIGURE 5. 4: Waveguide "T" Junction Terminated with its Characteristic Impedance and a Movable Short in the Two Arms	61
FIGURE 5. 5: Plot of Impedance Variation with Movement of Short, For the Waveguide Circuit of Fig. 5.4	61
FIGURE 5. 6: Rieke Diagram of the Oscillator	64

FIGURE 5. 7:	Small-Signal Electronic Admittance Y_{e1} vs Bias Voltage ($V < V_B$), Electronic Admittance Y_{e2} vs Output Power for Constant Frequencies	68
FIGURE 5. 8:	Change of Load Power and Frequency as a Function of Slide Screw Tuner Position	70
FIGURE 5. 9:	A Typical Frequency Spectrum Before a Frequency Jump	71
FIGURE 5.10:	Change of Frequency with Bias Current for a Given Load	72
FIGURE 5.11:	Change of Power with Bias Current for a Given Load	73
FIGURE 5.12:	Circuit Admittance as a Function of Frequency	74
FIGURE 5.13:	Change of Diode Admittance as a Function of Diode Current for a Given Load	75

CHAPTER I

INTRODUCTION

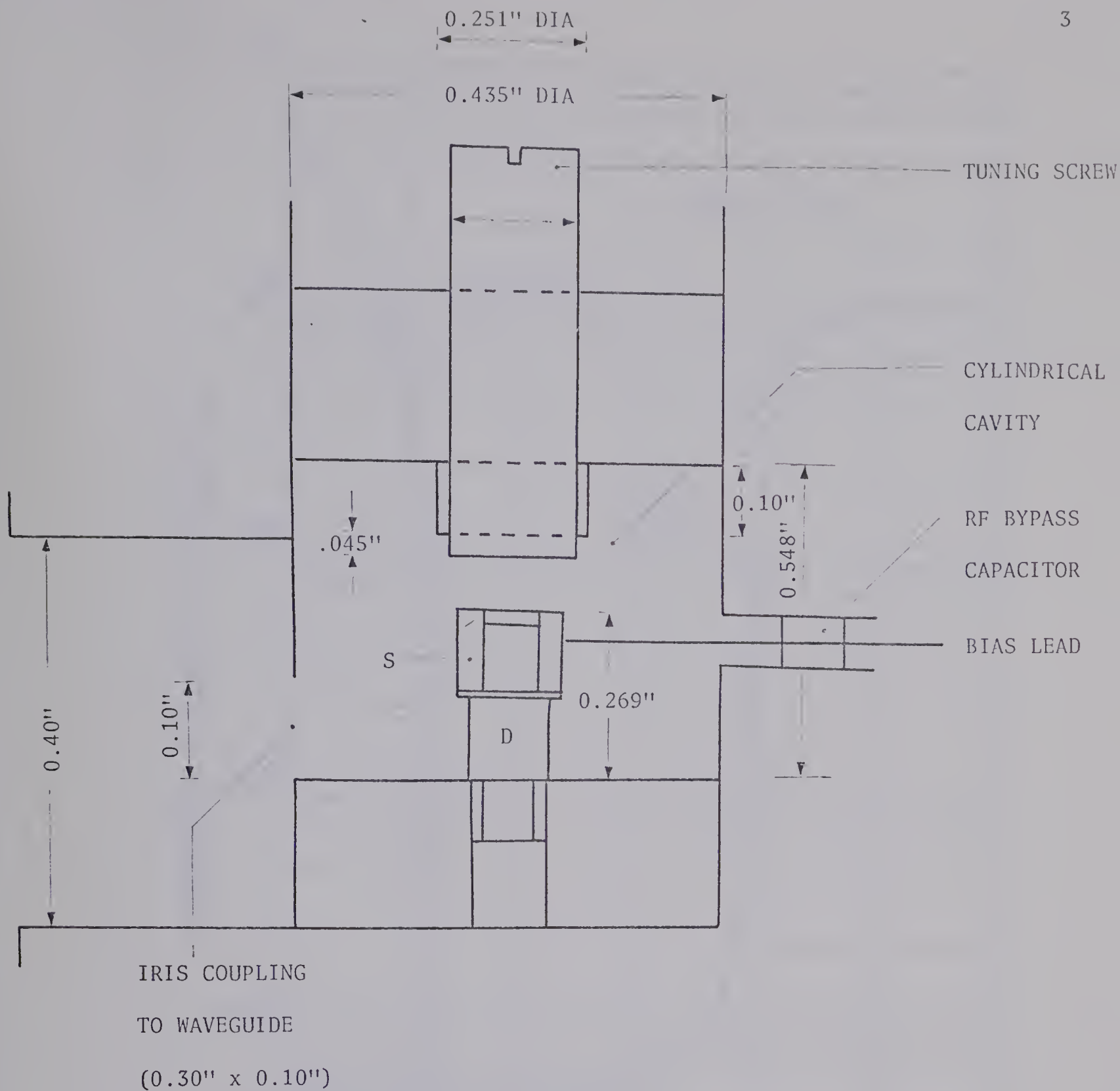
Semiconductor microwave devices have made tremendous headway¹ in the past ten years or so. Among these devices are IMPATT (IMPact Avalanche and Transit Time) diodes first proposed by Read² in 1958. However, several years elapsed before Johnston, et al.³ demonstrated the generation of microwave power by avalanching p-n junctions, which were not of a Read structure. Soon afterwards, Lee et al.⁴ experimentally demonstrated the feasibility of the Read structure.

The diode structure that Read proposed and analysed consists of a very narrow avalanche region followed by a drift region where charge carriers move with scattering-limited velocities. The combined phase-delay of current in these two regions results in a negative resistance, which permits such a diode to operate as a microwave generator.

Gilden and Hines⁵ used the space-charge approach to derive a small-signal equivalent circuit and explained electronic tuning effects in the Read diode. Gummel and Scharfetter⁶ carried this work further by including phase-shifts in the avalanche region and by using realistic values for the ionization coefficients ($\alpha \neq \beta$ in silicon); they obtained plots of admittance as a function of frequency and current density for different diode structures. From the first report of successful operation³ and later, from the work of Misawa⁷ and others, it may be concluded that structures other than that proposed by Read also possess negative conductance due to their transit time properties. Misawa showed that the negative resistance effect of the IMPATT type is

possessed also by a junction diode with a general doping profile, regardless of whether the doping profile is designed to localise the avalanche region (p-n-i-n) or to spread it uniformly (p-i-n). Johnson⁸ analysed the Read diode by considering different ionization coefficients for holes and electrons in silicon and obtained the small-signal admittance. For the large-signal case, a closed-form solution of the nonlinear equations describing a Read-type IMPATT diode was found by Evans and Haddad⁹, who also derived results on rf output power and efficiency. Later, Scharfetter and Gummel¹⁰ employed a simplified theory as a starting design for a silicon, p-n-v-n type Read diode and wrote a computer program for obtaining numerical solution of the equations of carrier transport, carrier generation and space-charge balance. They presented large-signal values of the diode admittance, diode average(dc) voltage and conversion efficiency as a function of ac voltage amplitude, for fixed average current density.

A microwave oscillator can be analysed by either one of the following two distinct approaches: (i) By studying the properties of charge carrier motion, the mechanism of dc - to - rf energy conversion and rf energy-transfer or (ii) by evolving appropriate equivalent circuits involving an electronic admittance. For this work, the second approach was adopted; the electronic admittance of an avalanche diode oscillator (ADO) has been determined experimentally¹¹. A cross-sectional view of the ADO is shown in Fig. 1.1. The doping profile of the commercially obtained diode used is shown in Fig. 1.2. The diode is a one-sided abrupt junction formed by diffusing a highly doped p-layer 2.6 microns deep into epitaxial silicon. The epitaxial layer is 7.7 microns thick and has an impurity density of approximately 5×10^{15}



LEGEND

S = SLEEVE

D = MCM PACKAGE
(CERAMIC MICROMIN)

FIG. 1.1. CROSS-SECTIONAL SKETCH OF AVALANCHE DIODE OSCILLATOR

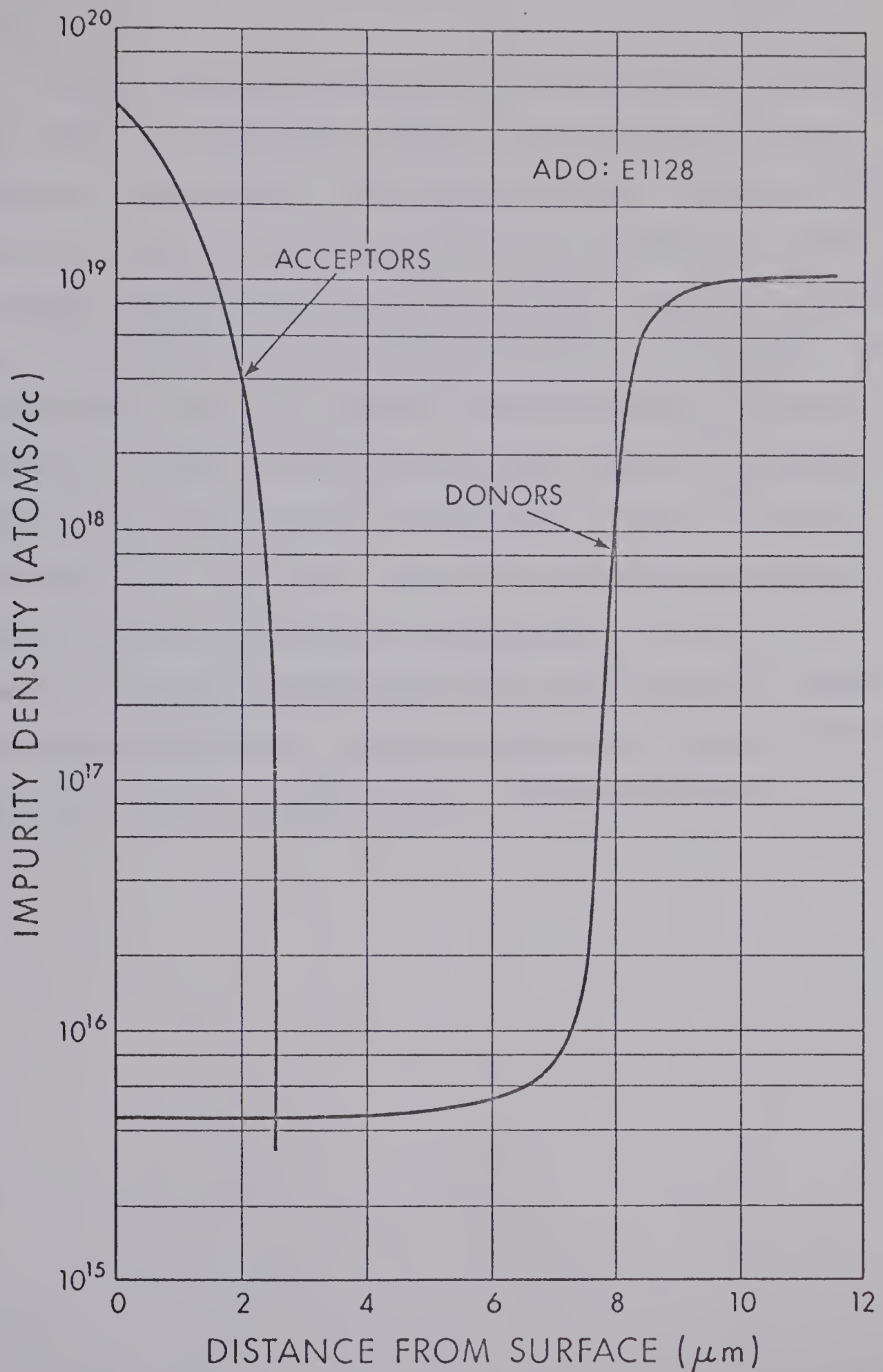


FIG.1.2. IMPURITY CONCENTRATION PROFILE OF SILICON AVALANCHE DIODE

atoms/cc.

First, the cavity housing the diode was characterized by cold-tests: That is, an equivalent circuit of the resonator and of the coupling iris was evaluated. Derivation of suitable equivalent circuits involves the study of the properties belonging to the complex consisting of resonator, output-coupler system and rf load. Therefore, in the next chapter, the resonator and its equivalent circuit are considered. After establishing the equivalent circuit, the ADO admittance was measured for various bias voltages less than the threshold voltage. The resonator admittance was subtracted from this admittance to obtain the small-signal admittance. Oscillator output power and frequency variation with load were studied with the aid of a reflectometer bridge, for cw operation. Measured load admittance values were then used to compute the electronic admittance. Frequency jumping with a change in load and bias current was also studied with the reflectometer bridge.

CHAPTER II

THE OSCILLATOR

CAVITY AND ITS OUTPUT-COUPLER SYSTEM

In this chapter, the choice of equivalent circuit representation for the cavity and for the coupling iris are described, along with the appropriate mathematical expressions. Various experimental techniques are then considered and finally the procedure for determination of the equivalent circuit outlined.

2.1 The Microwave Resonator and its Parameters

Because the ordinary concepts of voltage, current and impedance lose their conventional meaning when a circuit component becomes comparable in size to the operating wavelength, the equivalent circuit representation of a microwave oscillator is not as explicit as that of low frequency circuits. For example, a resonant circuit at low frequencies can be completely described by specification of the lumped parameters L , C and R . However, for a definition of the parameters of a microwave cavity resonator, a proper choice of field quantities relevant to the problem is necessary. Many practical cavities possess simple geometrical shapes. The stored magnetic and electric energies in the electromagnetic field determine the equivalent inductance and capacitance. Ohmic losses in the resonator walls and dielectric losses in the cavity determine its equivalent conductance. A low frequency resonant circuit comprised of lumped elements L , C and R possesses a single resonant frequency, whereas a cavity resonator can resonate at an

infinite number of frequencies. An accurate equivalent circuit representation of a microwave cavity without excessive losses, coupled by some arbitrary transducer to a waveguide, is shown in Fig. 2.1.

The shunt resonant circuits, of resonant frequencies $f_0, f_{01}, f_{02}, \dots, f_{0n}$, represent the resonant modes of the microwave cavity. The load admittance $G_\ell + jB_\ell$ is coupled to each of the resonator modes by the mutual inductance M_n of a coupling element, an iris in our case, having a self-inductance L_1 . Electronic activity within the cavity can excite these modes and is characterized by admittances $(G_{e0} + jB_{e0}), (G_{e1} + jB_{e1}), \dots, (G_{en} + jB_{en})$. The electronic admittances $(G_{em} + jB_{em})$ are defined as the ratio of rf current to rf voltage at the appropriate terminal pair; that is,

$$Y_{em} = G_{em} + jB_{em} = \frac{(i_{rf})_m}{(V_{rf})_m},$$

$$m = 0, 1, 2, \dots, n.$$

Resonators for oscillators are normally designed to possess fairly well-separated modes, permitting oscillations only in the vicinity of the desired frequency. The behaviour of a resonator near the selected frequency may thus be represented by retaining part of the equivalent circuit representing this mode, Fig. 2.2. In this diagram:

G_r = shunt conductance of the cavity

L_r, C_r = equivalent inductance and capacitance

L_1 = equivalent inductance of the coupling iris

M = mutual inductance between L_1 and L_r .

The diode package- and bias circuit losses and reactances are lumped with those of the cavity, since the diode is mounted inside the

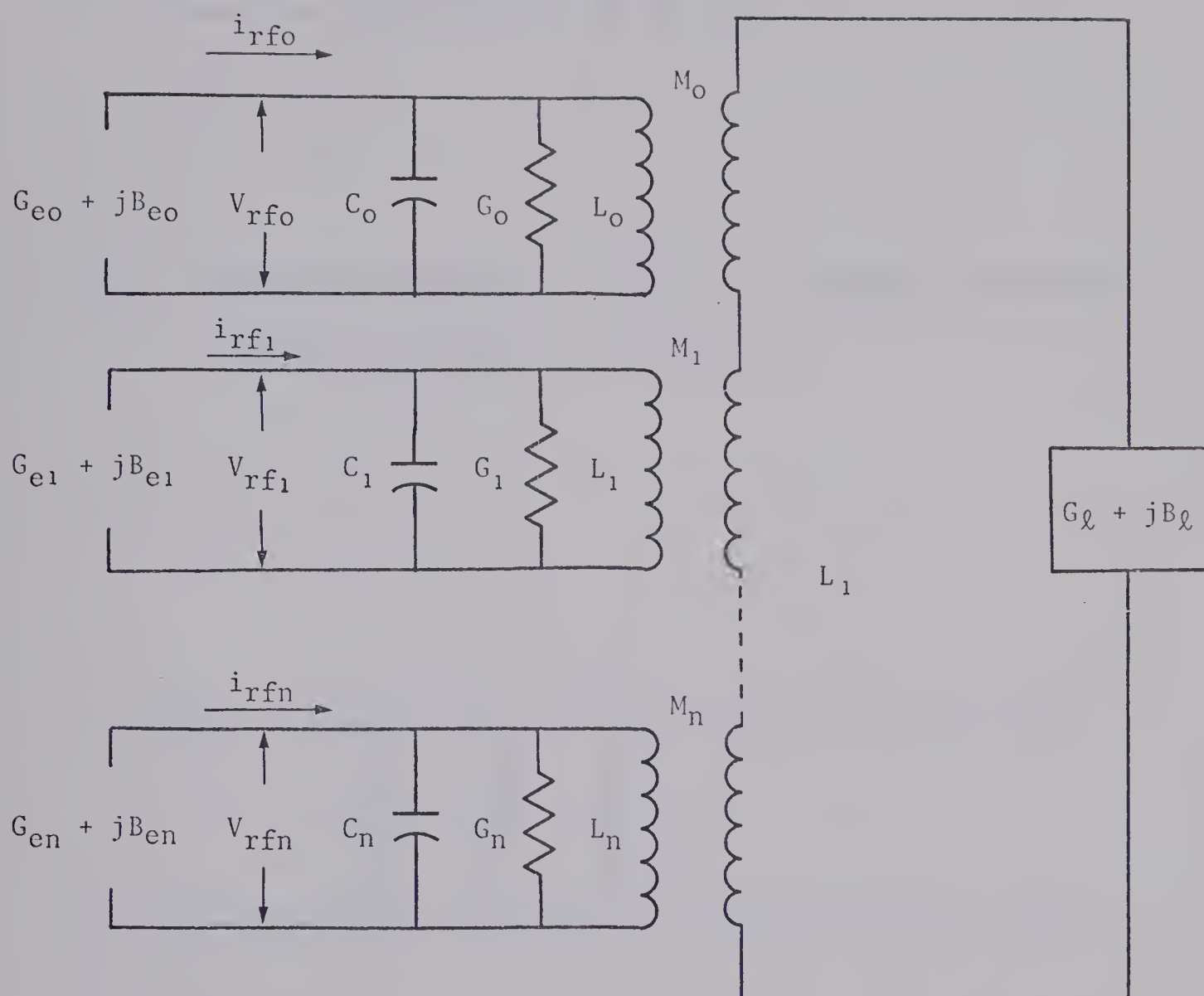


FIG. 2.1. EQUIVALENT CIRCUIT REPRESENTATION OF A MICROWAVE OSCILLATOR.

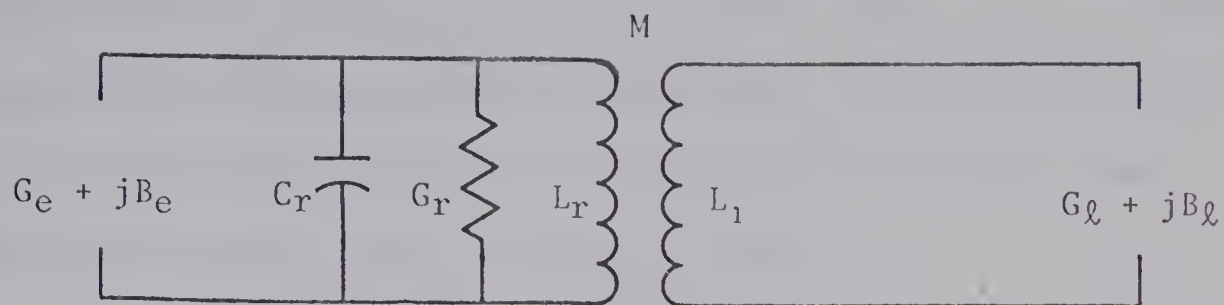


FIG. 2.2. SIMPLIFIED EQUIVALENT CIRCUIT OF A MICROWAVE OSCILLATOR
DESIGNED TO OPERATE IN A SINGLE MODE.

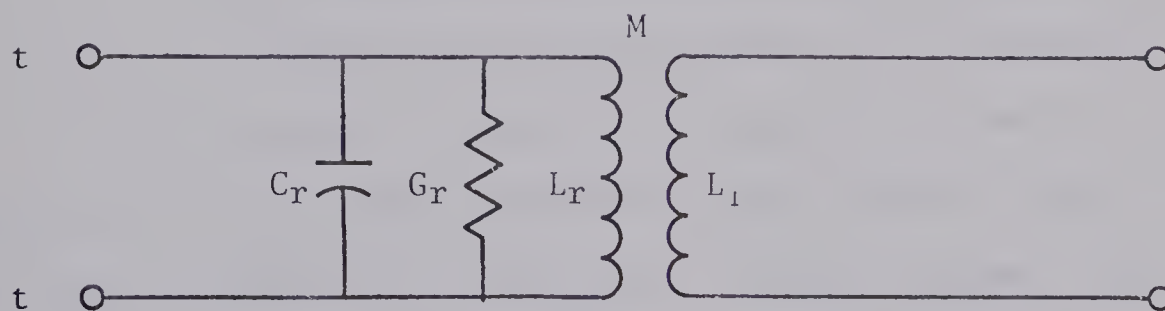


FIG. 2.3. EQUIVALENT CIRCUIT OF A MICROWAVE OSCILLATOR
IN "COLD" STATE.

cavity. When the operating voltage is reduced to zero, the device is in the "cold" state, and $(G_e + jB_e)$ are absent. Under these two conditions the equivalent circuit representation of Fig. 2.2 then reduces to Fig. 2.3, which then represents an iris-coupled avalanche diode oscillator when it is not generating a signal.

The circuit description of a cavity resonating in a given mode, as represented in Fig. 2.3, is complete if f_o , C_r and Q_o , the resonant frequency, resonator capacitance, and unloaded Q respectively, are known. As the ordinary concept of current and voltage does not hold at microwave frequencies, the shunt conductance is defined as

$$G_r = \frac{2W}{(\int E d\ell)^2} \quad \dots(2.1)$$

where

W = power dissipated in the cavity

E = the peak electric field along the path of integration
between two specified points in the resonator.

It is possible to obtain the theoretical parameters ω_o , Q_o , G_r , C_r and L_r for a few simple geometrical shapes from the losses in the walls and from geometrical factors but, for the resonator under consideration, mathematical computation would be too involved. Moreover, wall losses are a function of surface roughness and degree of tarnishing in addition to conductance of material and are best determined by experiment.

The following sections of this chapter deal with the procedure for the determination of L_r , C_r , G_r , L_1 and M of the actual resonator used.

The parameters of a resonant cavity L_r and C_r cannot be

measured directly in a distributed-element resonator like the one under investigation. The quantities that are directly measurable are the resonant frequency f_0 and the Q-value of the cavity. Q of a cavity may be defined by,

$$Q_0 = 2\pi \times \frac{\text{energy stored in cavity}}{\text{energy dissipated in cavity per cycle}} \bigg|_{\text{at resonance}}$$

This leads to the expressions:

$$Q_0 = (\omega_0 C_r) / G_r = 1 / (\omega_0 L_r G_r) \quad \dots(2.2)$$

where

$$\omega_0 = 2\pi f_0 = 1 / (L_r C_r)^{1/2} \quad \dots(2.3)$$

2.2 Determination of Equivalent Resonator Capacitance and Inductance

There are at least two different ways of determining C_r and L_r .

(1) Smith's Method¹²

(2) Differential Capacitance Variation Method¹³

(1) Smith's Method

Smith determined the numerical value of L_r for a magnetron resonator. He pointed out that if a capacitance ΔC is connected at the terminals t-t of Fig. 2.3, the square of the resonant wavelength λ_0 , should vary linearly with ΔC , and then from the equation¹²

$$\Delta(\lambda_0)^2 = (2\pi c)^2 L_r \Delta C \quad \dots(2.4)$$

L_r can be found. In his experiments, ΔC was the incremental change in capacitance of the resonator slots produced by filling the slots with a material of known dielectric constant.

This method may be adapted to determine L_r of an avalanche diode oscillator cavity either by filling the cavity with powdered

material- or with a liquid of known dielectric constant, and noting the change in resonant frequency.

This method was not used, as the second method was much more convenient for our application.

(2) Differential Capacitance Variation Method

In this method, it is assumed that the cavity as seen from the diode junction can be represented by a simple parallel resonant circuit. Furthermore, the diode package- and bias circuit losses and reactances are lumped with those of the cavity, as the diode is mounted in the actual physical structure of the oscillator. Then, with these assumptions,

$$Q_0 = \omega_0 C_r / G_r \quad \dots (2.5)$$

Q_0 and ω_0 are determined with the diode in position and with zero bias across the diode (but with the power supply switched on). Now it is possible to characterize the cavity so that C_r , G_r , L_r , M and L_1 are known.

The apparatus was connected as shown in Fig. 3.1 and the diode capacitance was measured with respect to an arbitrary reference level for various bias voltages. Later, resonant frequencies of the cavity corresponding to the same bias voltages were determined. Thus various resonant frequencies are known for corresponding measured decrements in diode capacitance.

Substituting the measured values of diode capacitance C_{ji} and their corresponding resonant frequencies f_i into the relation

$$\left(\frac{f_1}{f_2} \right)^2 = \left(\frac{C_{j2} + C_r}{C_{j1} + C_r} \right) \quad \dots (2.6)$$

the value of C_R was determined. G_R was then calculated from Eq. (2.5) and L_R obtained from $L_R = 1/(\omega_0^2 C_R)$.

2.3 Procedure for the Evaluation of the Coupling-System Parameters

The equivalent circuit for an iris-coupled avalanche diode oscillator at the plane of the iris is shown in Fig. 2.3. The coupling iris is here represented by a transformer. The transformer, consisting of the resonator inductance L_R and self-inductance (L_1) of the coupling iris, may be replaced by an ideal transformer of turns ratio (L_R/M) and a series secondary inductance L_2 of value $L_1(1 - M^2/L_1 L_R)$, as shown in Fig. 2.4. Now,

$$\begin{aligned} Y_R &= G_R + j\left(\omega C_R - \frac{1}{\omega L_R}\right) \\ &= G_R + j\omega C_R\left(1 - \frac{1}{\omega^2 L_R C_R}\right) \\ &= G_R \left[1 + j\frac{\omega C_R}{G_R}\left(1 - \frac{\omega_0^2}{\omega^2}\right)\right]. \end{aligned}$$

If the Q-value is appreciable then for ω in the vicinity of ω_0 ,

$$Y_R = G_R \left[1 + j2Q_0\left(\frac{\omega - \omega_0}{\omega}\right)\right] \quad \dots(2.7)$$

Therefore, (see Figs. 2.4 and 2.5),

$$\frac{1}{Z} = \frac{1}{(L_R/M)^2 Y_R} + j\omega L_2 \quad \dots(2.8)$$

Let

$$m = M/L_R \quad \dots(2.9)$$

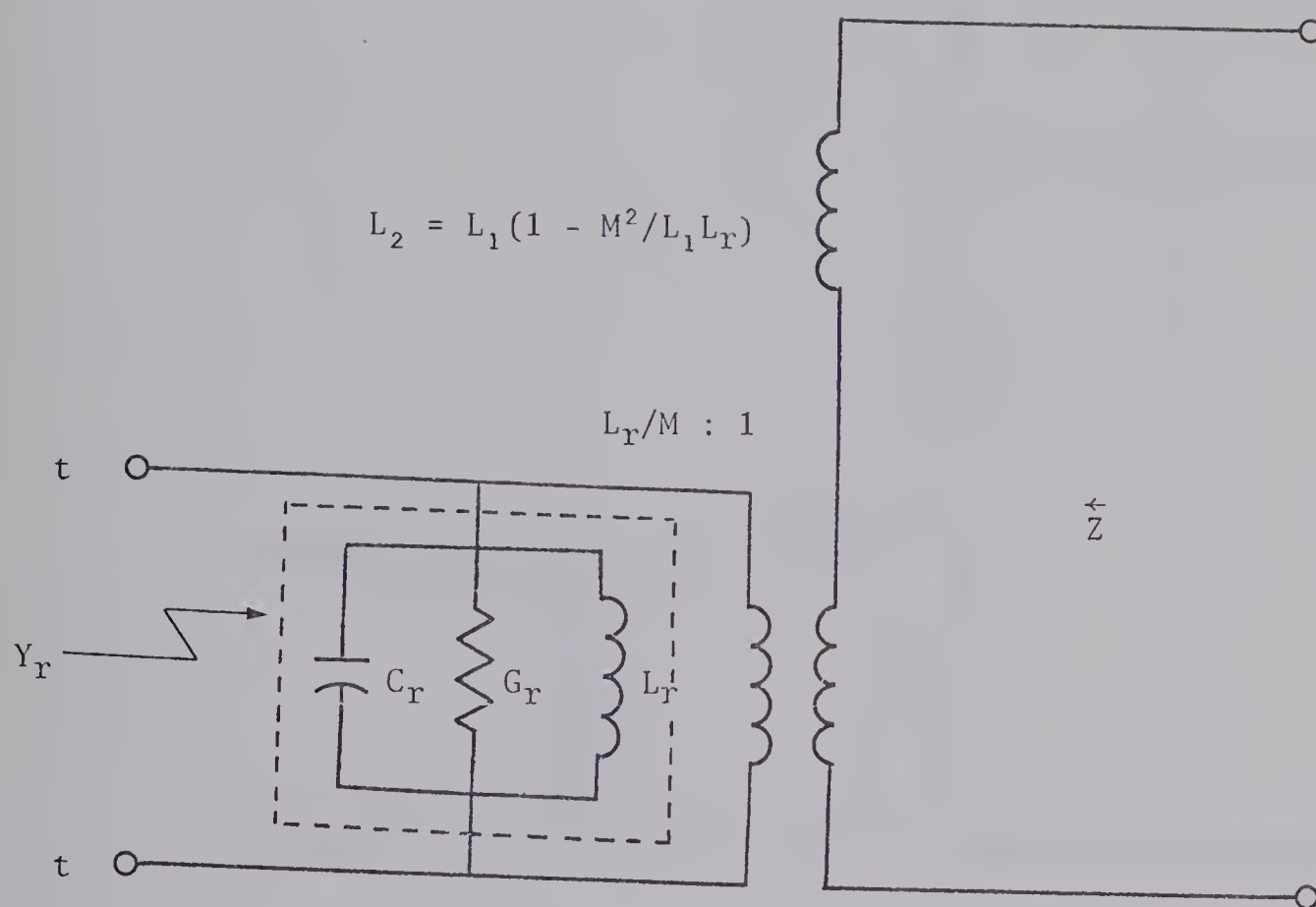


FIG. 2.4. EQUIVALENT CIRCUIT FOR THE AVALANCHE DIODE OSCILLATOR OF FIG. 2.3; THE TRANSFORMER IN FIG. 2.3 REPLACED BY AN IDEAL TRANSFORMER AND A SERIES SECONDARY INDUCTANCE L_2 .

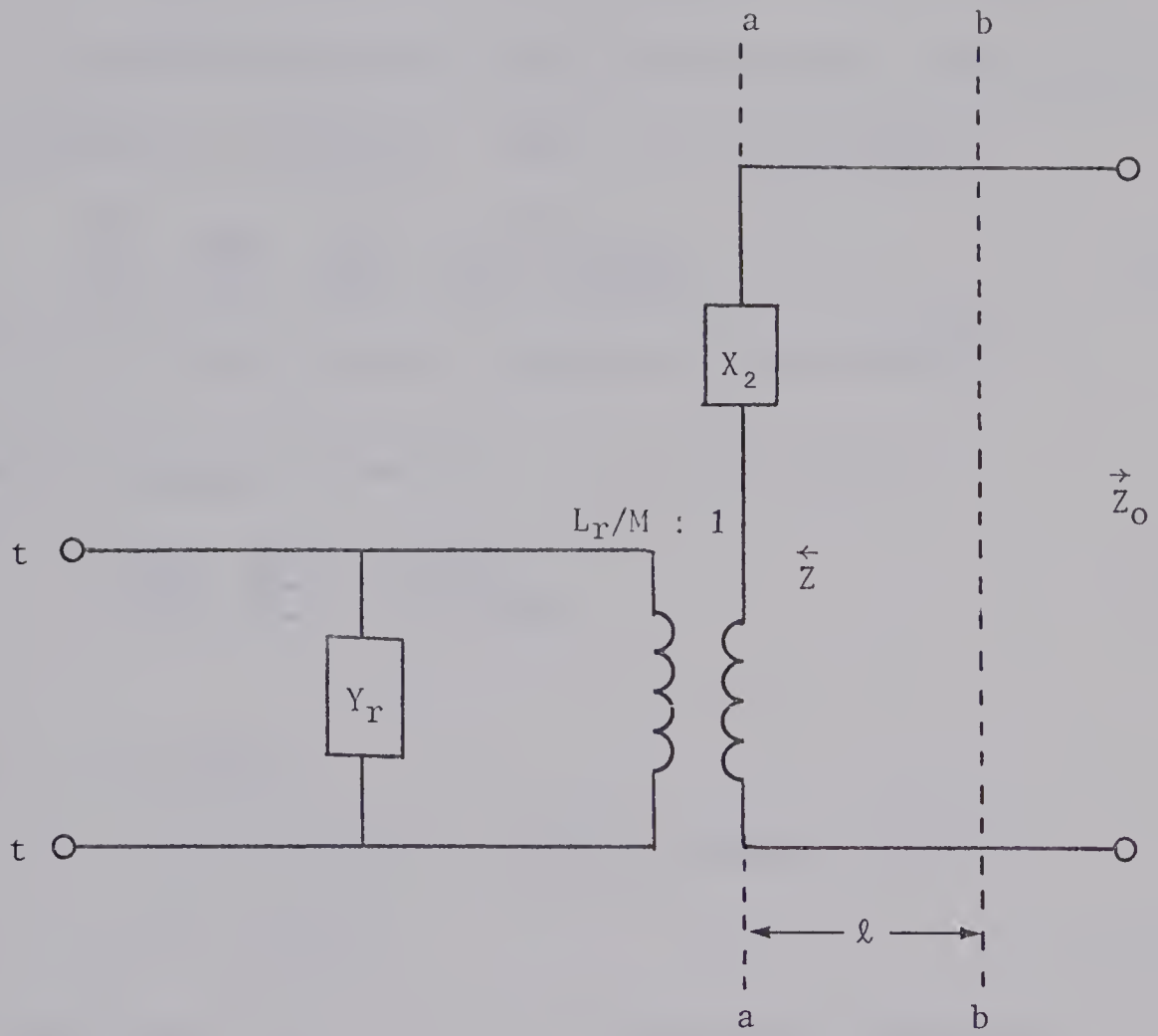


FIG. 2.5. EQUIVALENT CIRCUIT OF AN AVALANCHE
DIODE OSCILLATOR.

Then Eq. (2.8) becomes,

$$\bar{Z} = j\omega L_2 + \frac{m^2}{G_R(1 + j2Q_0\delta)} \quad \dots(2.10)$$

where

$$\delta = (\omega - \omega_0)/\omega, \text{ is the frequency tuning parameter.}$$

Since VSWR measurements give the equivalent circuit parameters it is convenient to normalise. Thus, Eq. (2.10) becomes

$$\frac{\bar{Z}}{Z_0} = \frac{Z_{aa}}{Z_0} = j\frac{X_2}{Z_0} + \frac{m^2/Z_0}{G_R(1 + j2Q_0\delta)} \quad \dots(2.11)$$

where Z_0 is the characteristic impedance of the waveguide.

In terms of coupling parameter β_1 , Eq. (2.11) becomes

$$\frac{Z_{aa}}{Z_0} = j\frac{X_2}{Z_0} + \frac{\beta_1}{(1 + j2Q_0\delta)} \quad \dots(2.12)$$

where

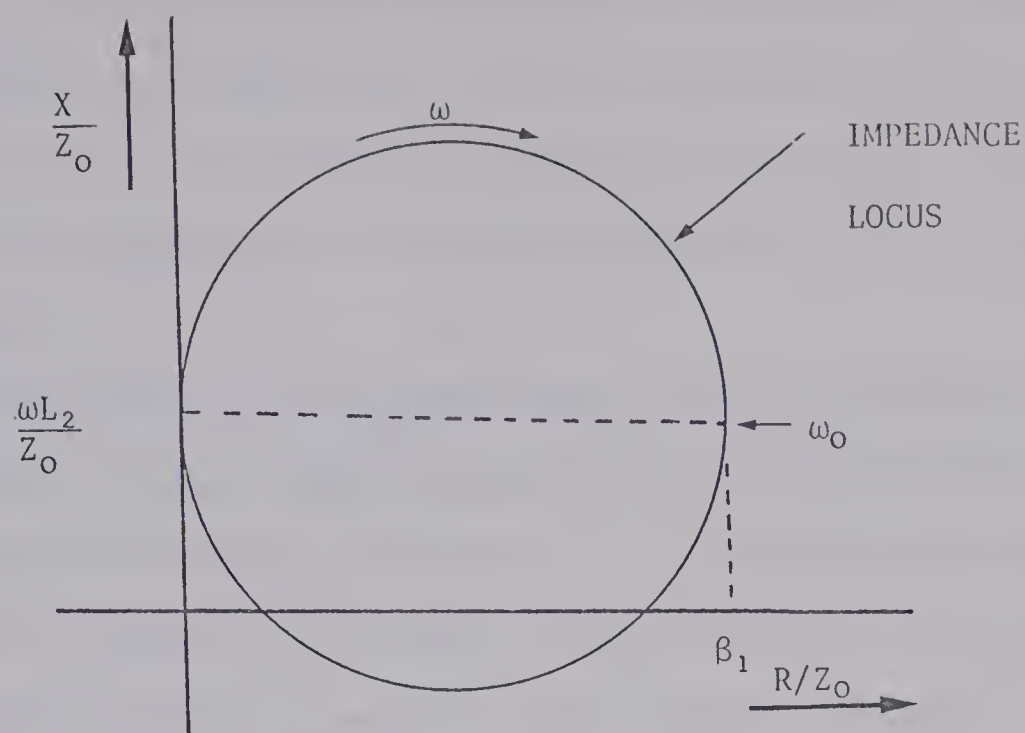
$$X_2 = \omega L_2$$

$$\delta = (\omega - \omega_0)/\omega = \text{frequency tuning parameter}$$

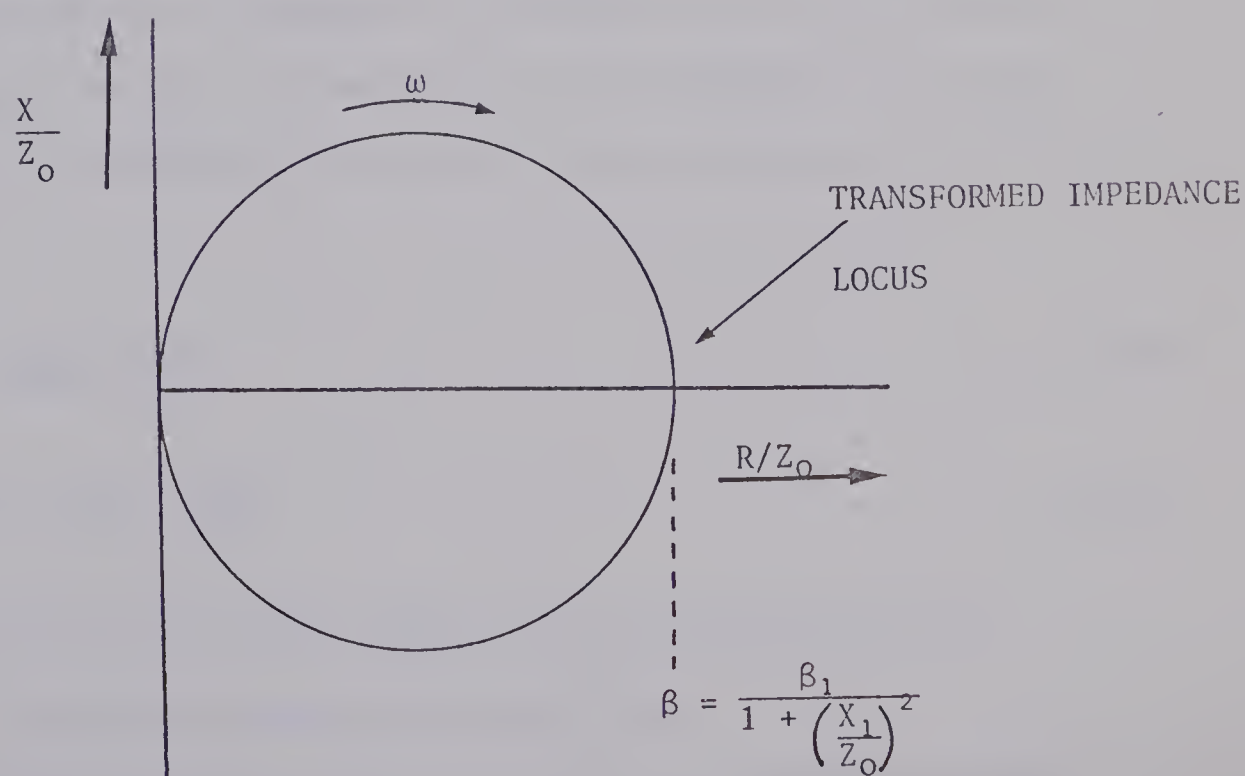
$$\beta_1 \approx m^2/G_R Z_0 \quad \dots(2.13)$$

The plot of Eq. (2.12) in the rectangular impedance plane is shown in Fig. 2.6(a). The circle is due to the second term in the right hand side of Eq. (2.12); it represents the impedance of a parallel resonant circuit, with the resonant impedance $\beta_1 Z_0$.

When the operating frequency is well removed from resonance, the second term in the right hand side of Eq. (2.12) becomes negligible, leaving the normalised reactance $(\omega L_2/Z_0)$ of the coupling transducer as the terminating load. As a result standing waves of large magnitude will exist in the waveguide connecting to the oscillator and the location of minima can be determined experimentally. For this purpose



(a)



(b)

FIG. 2.6. INPUT IMPEDANCE OF RESONATOR. (a) THE INPUT IMPEDANCE REFERRED TO PLANE a-a NEAR RESONANT CAVITY; (b) THE IMPEDANCE LOCUS REFERRED TO THE DETUNED SHORT POSITION.

the position of the voltage node for different frequencies was noted and the node shifts observed when the cavity was replaced by a short. The plot of these values on a Smith chart gave values of $(\omega L_2/Z_0)$, L_2 's were then calculated and the average value was $0.557 \times 10^{-9}H$. Thus L_2 can be measured.

If the plane of the "detuned-short" were to be chosen as the reference-plane, the term representing the self-reactance of the coupling-system is eliminated. The cavity, as seen from the detuned-short position, appears to be a shunt resonant circuit. Let the distance between reference planes a-a and b-b be " ℓ ", then the resonator impedance at a-a transformed to b-b is

$$\frac{Z_{bb}}{Z_0} = \frac{Z_{aa} + jZ_0 \tan \beta \ell}{Z_0 + jZ_{aa} \tan \beta \ell} \quad \dots(2.14)$$

The location of b-b is so chosen that when the cavity is detuned the impedance at terminals b-b vanishes. $Z_{aa} = jX_2$ when the cavity is detuned or when the measuring signal frequency is far off resonance. By the conditional selection of the reference plane b-b, $Z_{bb} = 0$ when

$$\tan \beta \ell = \frac{-X_2}{Z_0} \quad \dots(2.15)$$

$$\text{or} \quad \beta \ell = \tan^{-1} \frac{X_2}{Z_0} \quad \dots(2.16)$$

β when used in relation to the expression $\tan \beta \ell$ represents the "propagation constant" in the transmission line.

From Eqs. (2.12), (2.14) and (2.16), the impedance as seen from the detuned short position for any value of δ transforms to

$$\frac{Z_{bb}}{Z_0} = \frac{\beta}{1 + j2Q_0(\delta - \delta_0)} \quad \dots(2.17)$$

where

$$\delta_0 = \frac{\beta}{2Q_0} \left(\frac{X_2}{Z_0} \right) \quad \dots(2.18)$$

This transformed impedance is that of a shunt circuit possessing a resonant impedance of βZ_0 . The plot of Eq. (2.17) in the impedance plane is again a circle, Fig. 2.6(b).

Recollecting:

$$m = M/L_R \quad \dots(2.9)$$

$$\frac{Z_{aa}}{Z_0} = jX_2 + \frac{\beta_1}{(1 + j2Q_0\delta)} \quad \dots(2.12)$$

$$\beta_1 = \frac{m^2}{G_R Z_0} = \frac{M^2}{L_R^2 G_R Z_0} \quad \dots(2.13)$$

From Eq. (2.17)

$$\beta = \frac{\beta_1}{1 + (X_2/Z_0)^2} \quad \dots(2.19)$$

We know C_R , L_2 and f_0 , Q_0 , are measurable by standard methods.

From the use of β and X_2 in

$$\beta_1 Z_0 = \beta Z_0 \left[1 + \left(\frac{X_2}{Z_0} \right)^2 \right]$$

$\beta_1 Z_0$ is calculated. From Eq. (2.13)

$$\begin{aligned} M^2 &= (\beta_1 Z_0) L_R^2 G_R \\ \text{or } M &= (\beta_1 Z_0)^{1/2} L_R (G_R)^{1/2} \end{aligned}$$

Thus M is calculable and when it is used in

$$L_2 = L_1 \left(1 - \frac{M^2}{L_1 L_R} \right)$$

or

$$L_1 = \left(L_2 + \frac{M^2}{L_R} \right)$$

L_1 can be computed.

Thus all the parameters of the equivalent circuit can be determined experimentally.

CHAPTER III

EXPERIMENTAL DETERMINATION OF THE OSCILLATOR EQUIVALENT CIRCUIT AND THE ELECTRONIC ADMITTANCE

In this chapter, the experimental determination of the resonator capacitance C_r is described. Also, measurements carried out to obtain f_0 , Q_0 , β and the consequent computation of G_r , L_r , M and L_1 are explained. Finally, the procedure used for obtaining the small-signal electronic admittance from circuit admittance plots at different bias voltages is described.

3.1 Measurement of Resonator Capacitance

The experimental set-up of Fig. 3.1 was used to determine the change in capacitance with bias voltage. External bias was superimposed on a 1MHz 15mV test signal from a Boonton Capacitance Bridge. The capacitance change of the avalanche diode oscillator (ADO) was measured by comparing this with a 25pF capacitor. To obtain the resonator capacitance by the use of Eq. (2.6), change in diode capacitance with voltage is required. The bridge was balanced with the ADO (in the cold-state) and a 25pF capacitor connected across its "DIFF" and "TEST" terminals respectively, and capacitance readings were taken for different bias voltages. With a change in the value of bias voltage, the diode capacitance changes but because the 25pF capacitance (across "TEST" terminals) is unvarying, a decrease in the diode capacitance shows up on the meter. Since the capacitance measurements were in the low pF range

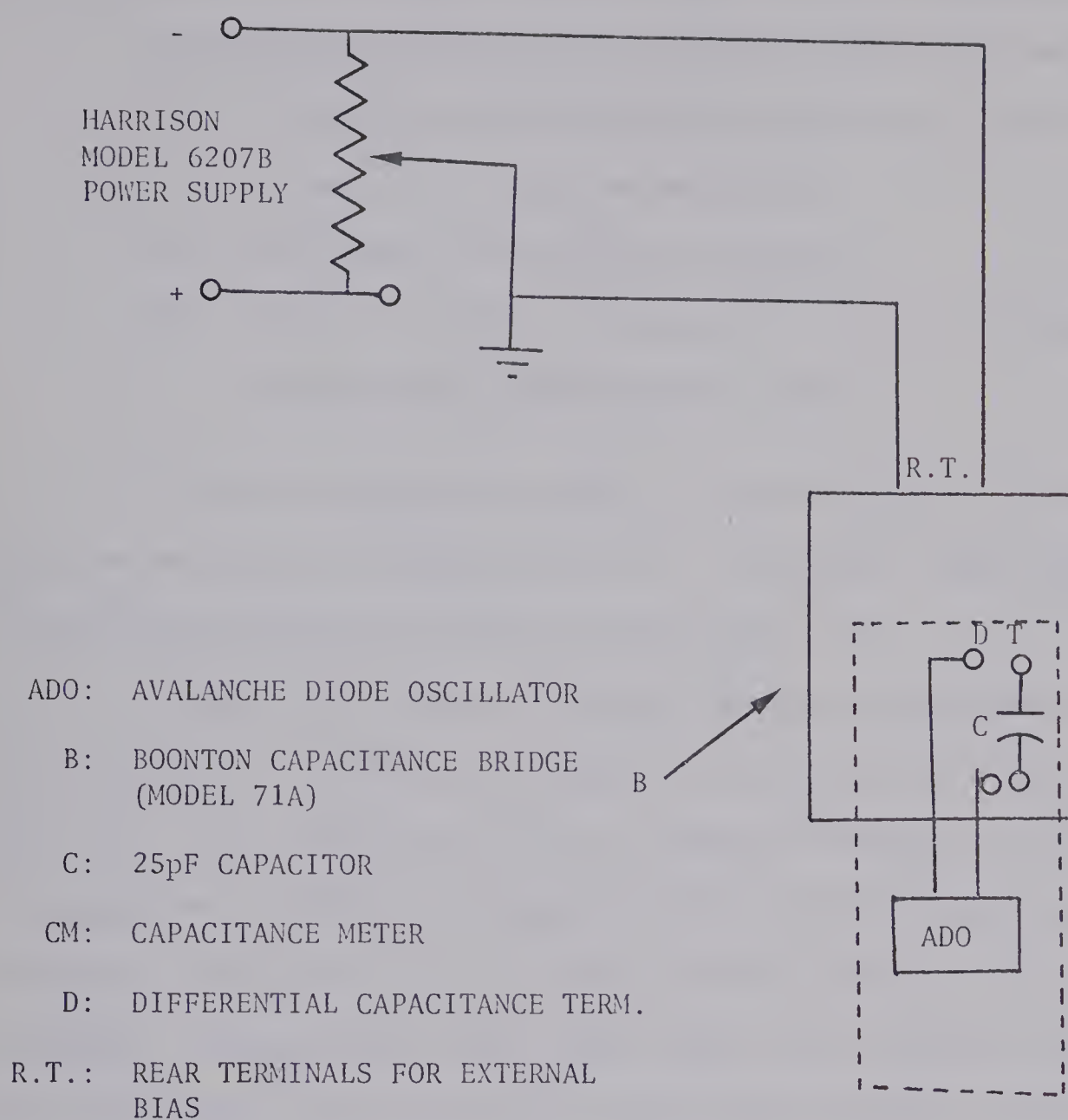


FIG. 3.1. EXPERIMENTAL SET-UP FOR MEASURING THE CHANGE IN
CAPACITANCE OF ADO WITH BIAS VOLTAGE.

it is necessary to shield the circuit. Suitable shielding was provided by a tin-foil box, in order that the results become reproducible.

The following procedure was followed in the measurements:

- (1) The above arrangement was set up, dc supply was switched on but zero voltage was maintained.
- (2) The capacitance bridge was balanced.
- (3) The bias current was increased in steps of 0.5V and the corresponding capacitance was noted.

A plot of capacitance change, C , versus bias voltage (with zero bias as reference) is shown in Fig. 3.2. De Loach¹⁴ showed that capacitance measured above may be used in Eq. (2.6).

In Fig. 3.2 a curve of resonant frequency versus bias voltage is also shown. This curve was obtained with the set-up illustrated in Fig. 3.3. For a fixed value of bias voltage the VSWR in the waveguide was measured at different frequencies with a signal incident on the resonator. These data yield a curve of VSWR vs frequency; the frequency corresponding to the lowest VSWR is the resonant frequency. This measurement was repeated for various bias voltages; the data, when plotted, give a curve of resonant frequency versus bias voltage, Fig. 3.2. Values of C_j , i.e. C_{j1} , C_{j2} , etc. for voltages V_1 , V_2 , etc. respectively, and corresponding values of f_1 , f_2 , etc. were observed. The values of bias voltage, change in diode capacitance and resonant frequency of the circuit are shown in Table 3.1.

Four values of resonator capacitance C_r were calculated by the use of Eq. (2.6) by using combinations of readings of Table 3.1. Measurements 1 and 5, 2 and 6, etc. were used and the results averaged giving $C_r = 6.24\text{pF}$.

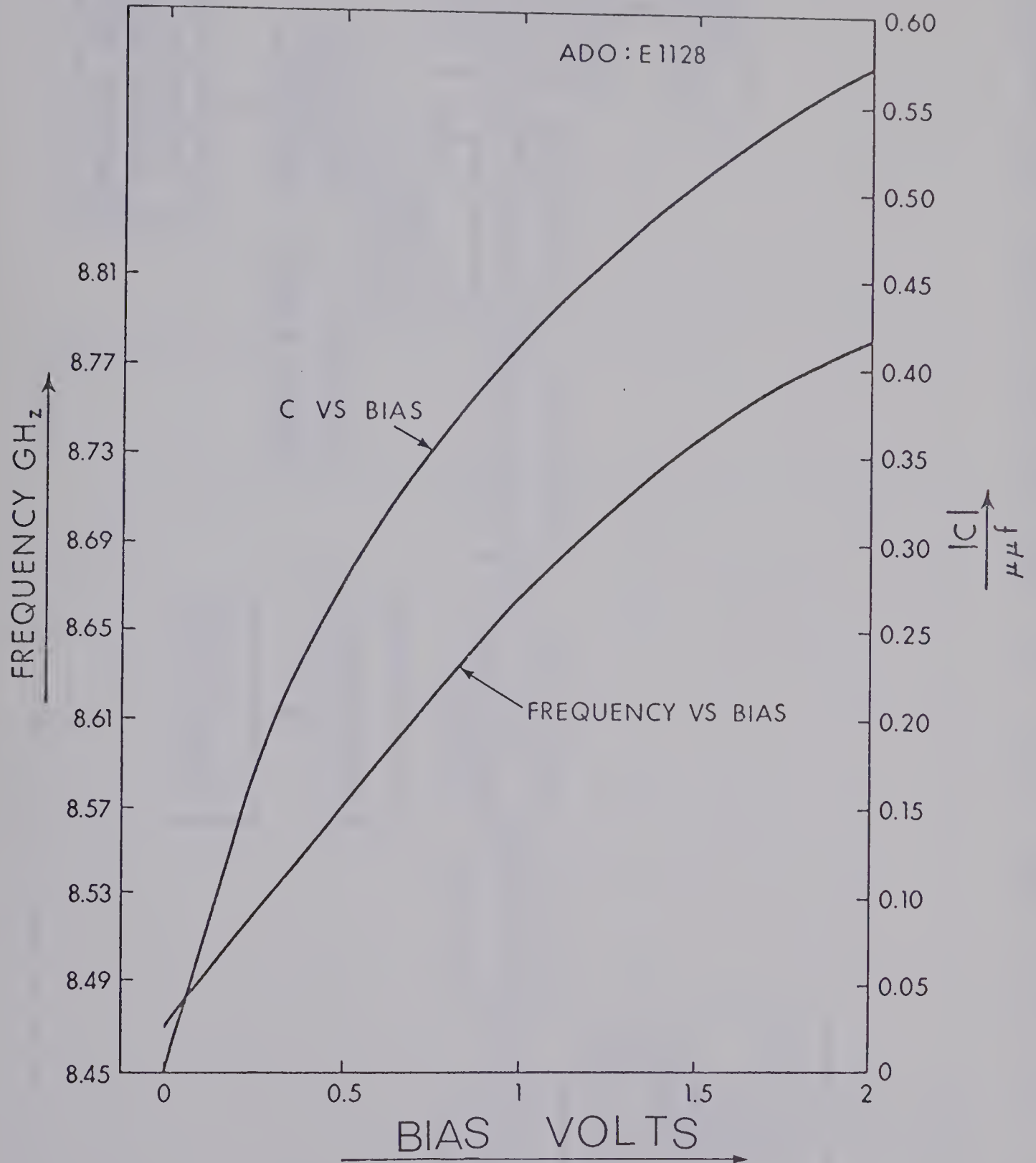


FIG. 3.2.

CHANGE OF DIODE CAPACITANCE AND OF CIRCUIT
RESONANT FREQUENCY WITH BIAS VOLTAGE

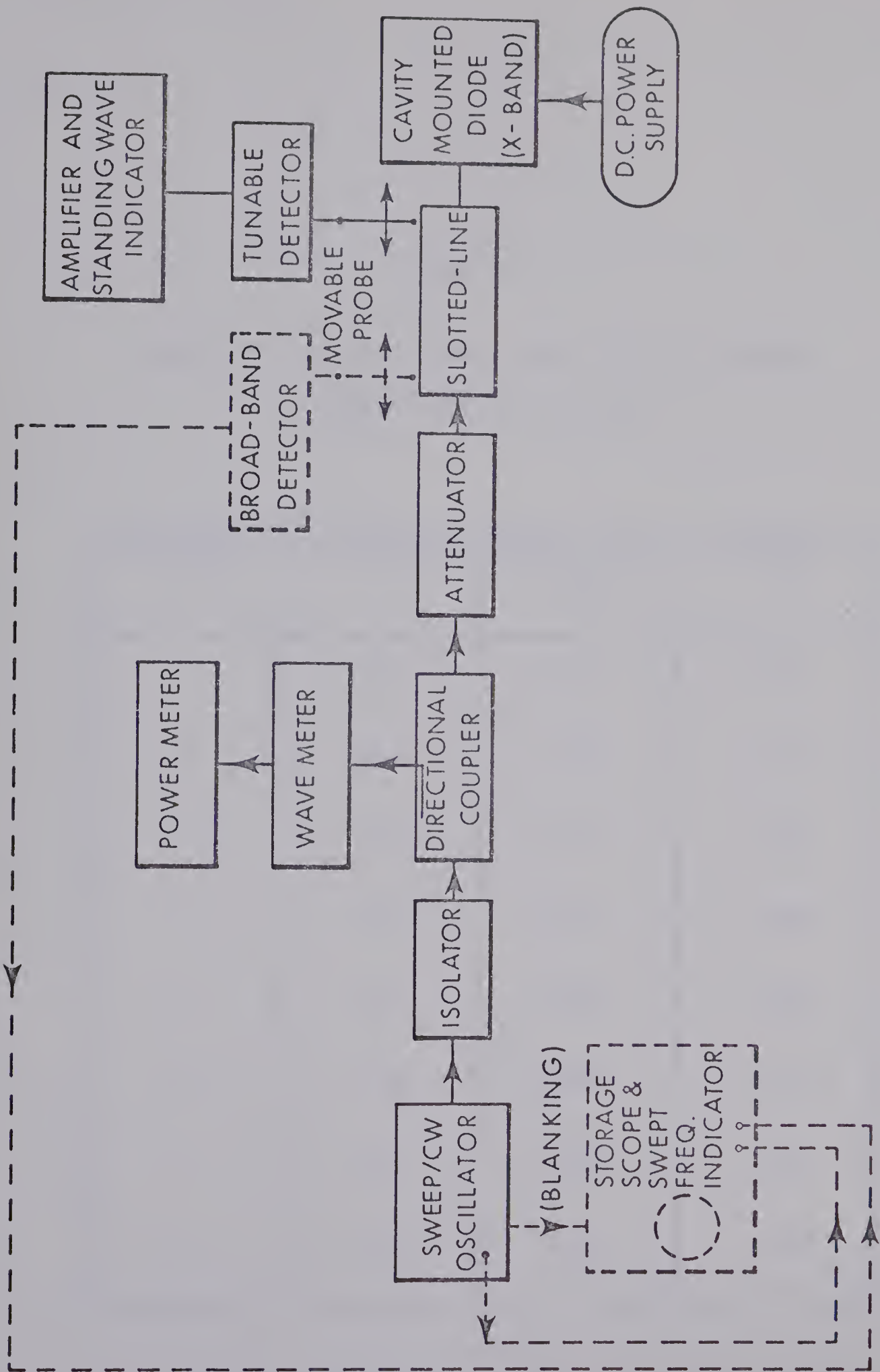


FIG. 3.3. CIRCUIT USE FOR COLD-TESTS ON AVALANCHE DIODE OSCILLATOR

TABLE 3.1

CHANGE OF DIODE CAPACITANCE AND OF CIRCUIT RESONANT
FREQUENCY WITH BIAS VOLTAGE

Measurement Number	Bias Voltage (volts)	Change in Capacitance (pF)	Frequency (GHz)
1	0.25	0.171	8.522
2	0.50	0.277	8.570
3	0.75	0.354	8.621
4	1.00	0.415	8.665
5	1.25	0.463	8.705
6	1.50	0.505	8.737
7	1.75	0.542	8.764
8	2.00	0.570	8.783

3.2 Measurement of Q_0

Many different techniques are available for experimentally determining the Q-value of a resonator; they may be grouped as¹⁵

- (1) Transmission Method
- (2) Impedance Measurement
- (3) Transient Decay or Decrement Method
- (4) Dynamic Method.

In the first method the cavity is employed as a transmission device; this method is precluded in our case, as the resonator under study is a one-port device.

The second method consists of an observation of the variation in resonator impedance as a function of frequency. If a cavity impedance is measured as a function of frequency, the impedance locus is a circle if referred to the plane of the detuned-short, and a straight line if referred to the plane of the detuned-open, Fig. 3.4. From these data the values of unloaded Q, Q_0 can be found. It is also possible to determine the resonator parameters from the VSWR measurements if the degree of coupling of the cavity to waveguide is known. A graph of VSWR versus frequency was used to determine the value of Q_0 .

The decrement method is suitable for cavities of high Q-value where it overcomes the need for a highly stable oscillator, but for cavities with low Q-values, as was the case for the one under observation, the decay period is too short for convenient measurement.

The solid-line section of Fig. 3.3 was the set-up used to perform "cold-tests" on the resonator. "The Impedance Method"¹⁵ was used to determine the resonator parameters. The cavity (housing the diode) under study was connected to the generator through a directional

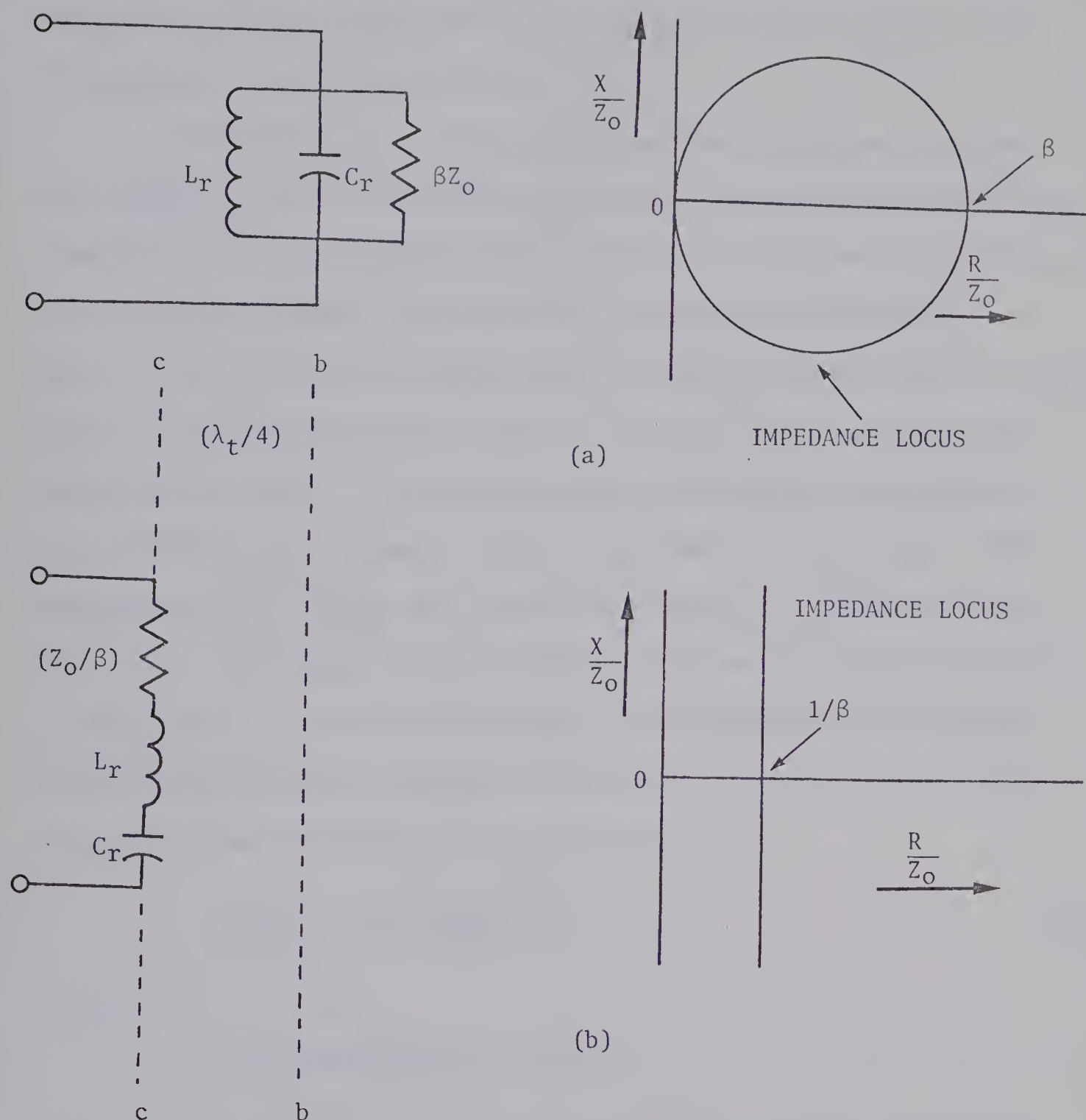


FIG. 3.4. PARALLEL AND SERIES EQUIVALENT REPRESENTATION OF A RESONANT CAVITY: THE EQUIVALENT IMPEDANCE REFERRED TO (a) THE PLANE OF DETUNED SHORT, (b) THE PLANE OF DETUNED OPEN WITH ACCOMPANYING IMPEDANCE PLANE PLOTS.

coupler, an attenuator (acting as a pad and level control) and a slotted-line. The directional coupler samples the incident wave for frequency and power measurement. The detector output goes from the slotted-line to a VSWR indicator.

To determine the value of Q_0 , the bias voltage of the diode was reduced to zero. Then VSWR and position of minimum were noted for incident signals of different frequencies. The position of the voltage node, in the waveguide, was plotted as a function of frequency, Fig. 3.5(a); there was a steady shift of nodal position toward the load with increasing frequencies, hence the cavity is overcoupled to the transmission line¹⁶. If the cavity were undercoupled, the curve of nodal shift versus frequency would be as shown in Fig. 3.5(b). The measured values of VSWR were plotted as a function of frequency, see Fig. 3.6. The minimum value of VSWR (=26) gives the value of coupling coefficient β . Moreover the frequency corresponding to this minimum VSWR is the resonance frequency of the cavity. The half power points $(r_{1/2})_0$ were found analytically by using Eq. (3.1)¹⁵,

$$(r_{1/2})_0 = \frac{2 + \beta^2 + \sqrt{4 + \beta^4}}{2\beta} \quad \dots(3.1)$$

where

β = coefficient of coupling.

By drawing a line parallel to the horizontal axis at a $VSWR = (r_{1/2})_0 = 26.04$, in Fig. 3.6 half power frequencies f_1 and f_2 were obtained, these were 8.456 GHz and 8.484 GHz respectively.

The value of Q_0 was then computed from:

$$Q_0 = \frac{f_0}{(f_2 - f_1)} = \frac{8.470}{(8.484 - 8.456)} = 306 \quad \dots(3.2)$$

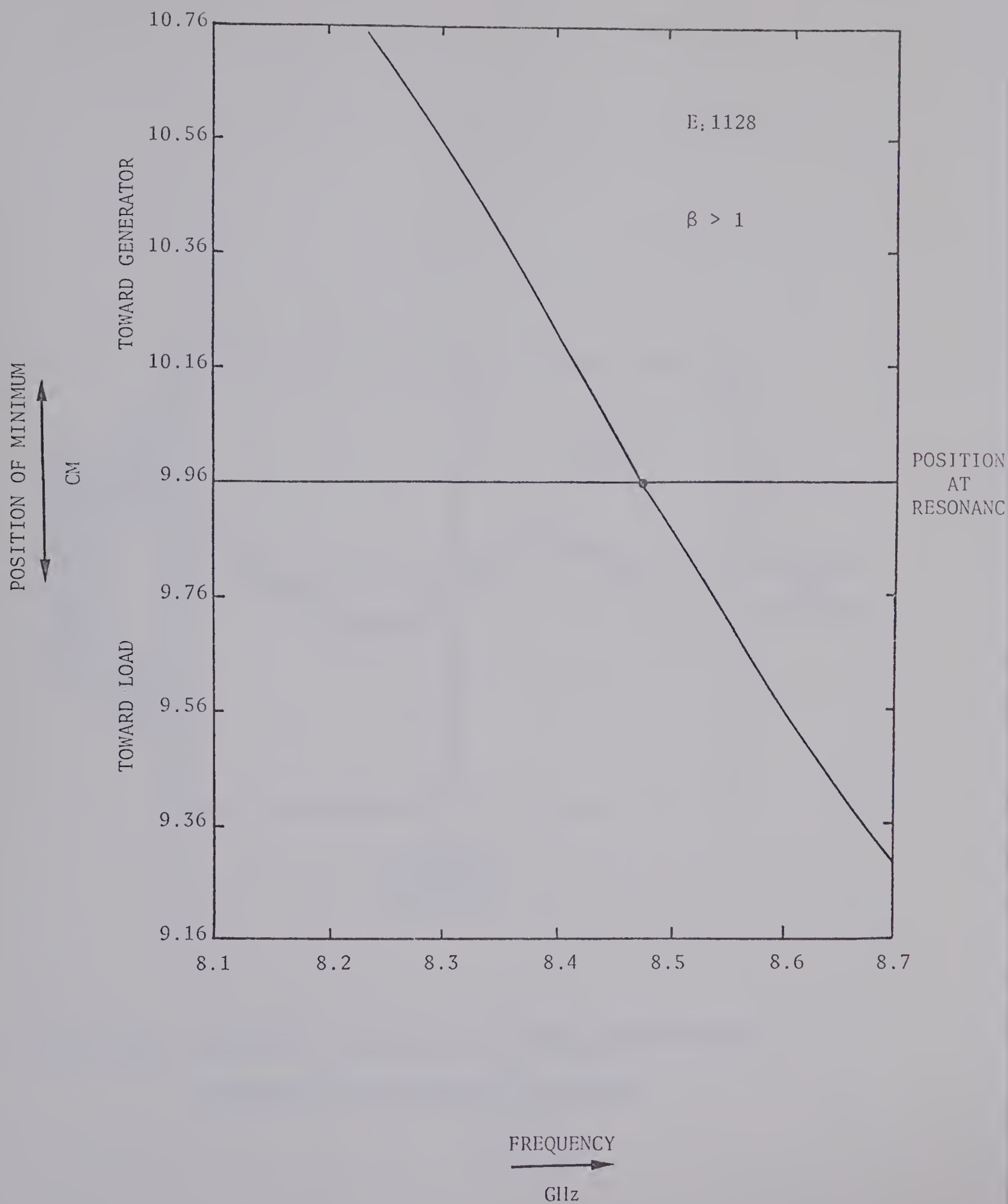


FIG. 3.5(a). VARIATION IN POSITION OF MINIMUM AROUND RESONANT FREQUENCY.

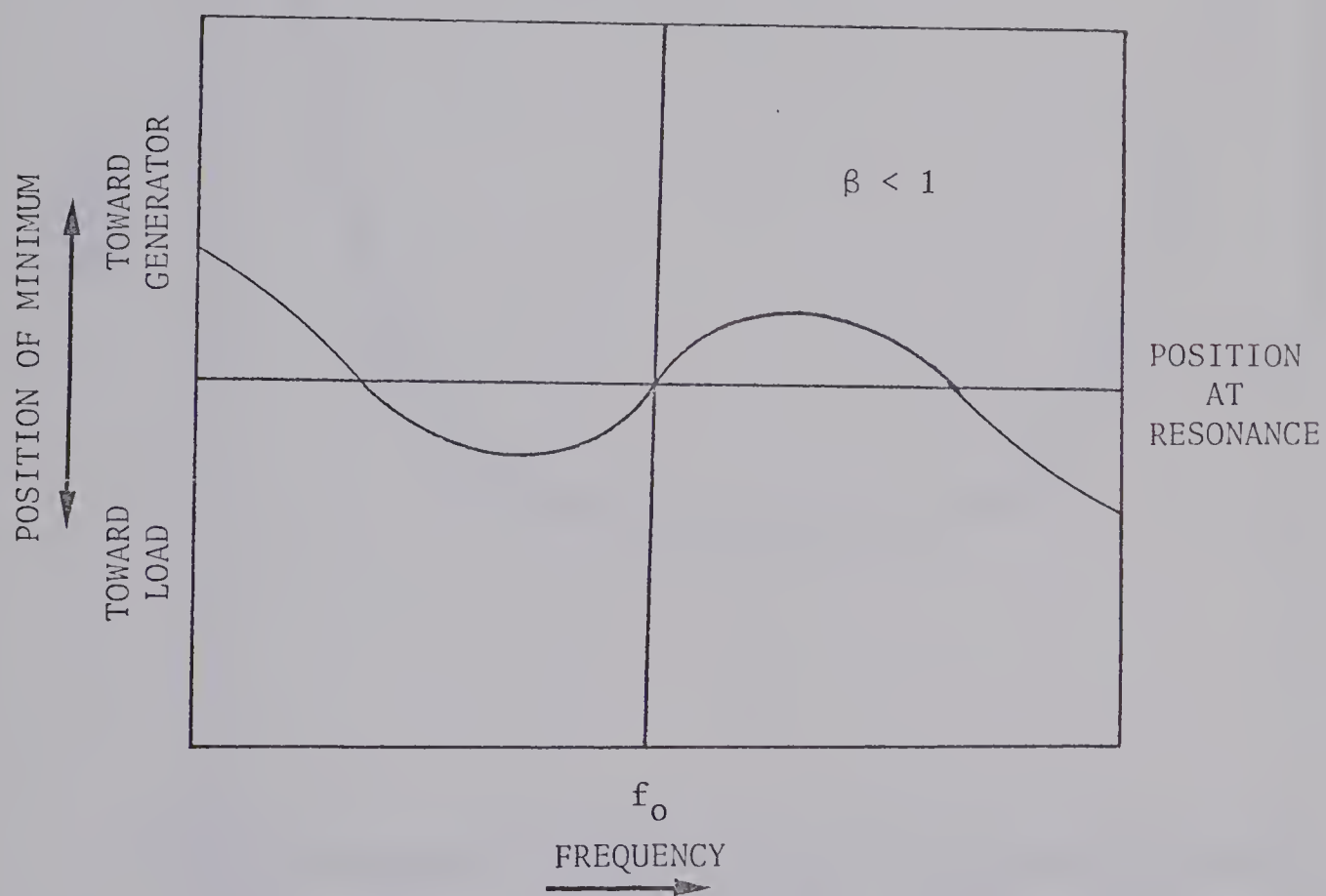


FIG. 3.5(b). VARIATION IN POSITION OF MINIMUM AROUND RESONANT FREQUENCY FOR AN UNDERCOUPLED CAVITY.

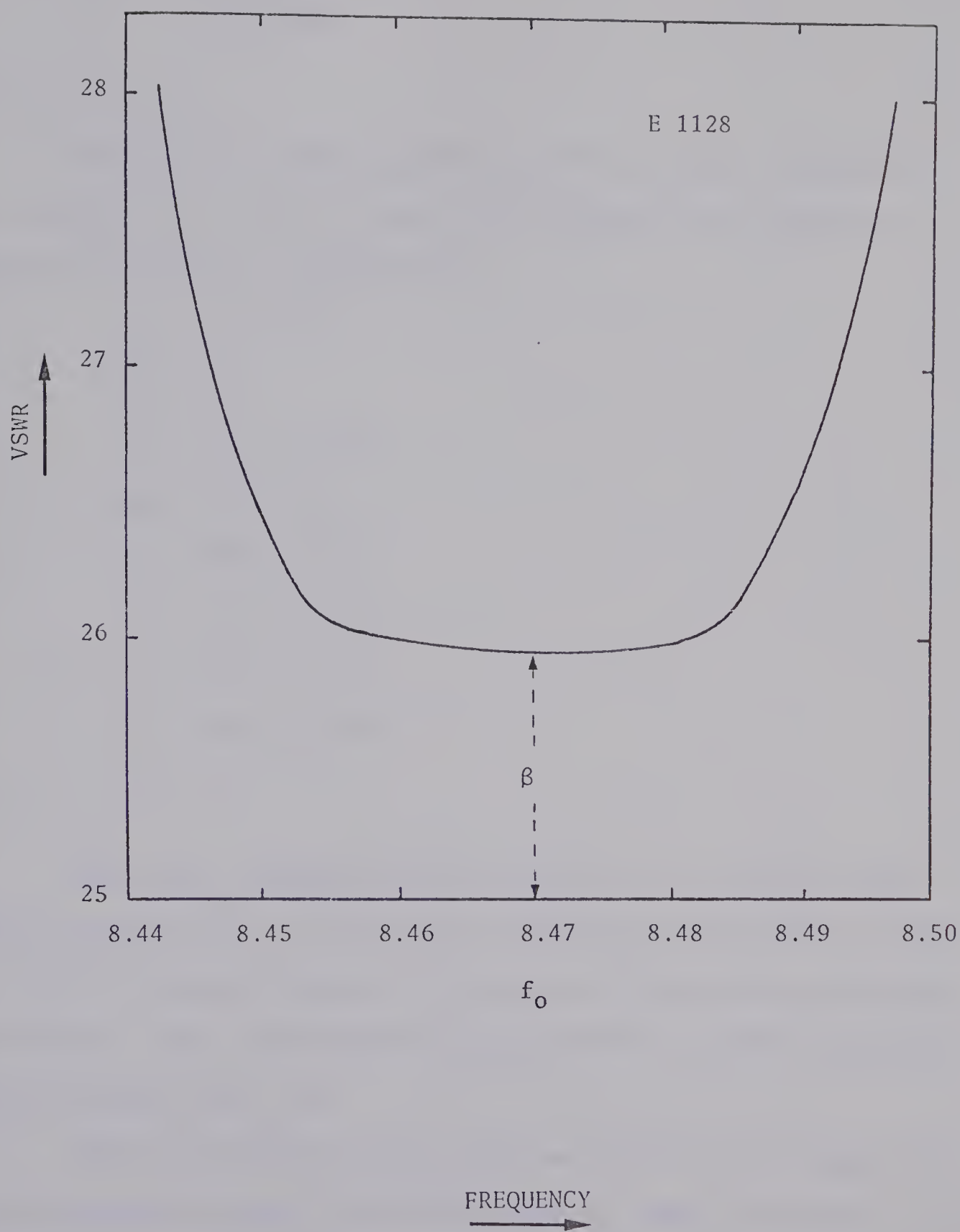


FIG. 3.6. VARIATION IN VSWR AROUND RESONANT FREQUENCY OF CAVITY.

where

Q_0 = unloaded Q of cavity

f_0 = resonant frequency of cavity

= 8.470 GHz.

Also, $C_r = 6.24$ pF.

Knowing these values and following the procedure outlined in Ch. 2, values of L_r , G_r , L_1 , L_2 and M were computed. The numerical values of the different parameters are:

$f_0 = 8.470$ GHz

$Q_0 = 306$

$C_r = 6.24 \times 10^{-12}$ F

$G_r = 0.0011$ mhos

$L_r = 56.5 \times 10^{-12}$ H

$L_1 = 1.22 \times 10^{-9}$ H

$L_2 = 0.557 \times 10^{-9}$ H

$M = 0.194 \times 10^{-9}$ H

$\beta = 26$.

VSWR versus frequency curves were plotted for different bias voltages (see Fig. 3.7). These curves indicate that the Q-value of the diode and the resonant frequency of the circuit increase with increasing bias voltage. Also, the resonant frequency of the oscillator increases with bias voltage, Fig. 3.8.

The input impedance of the diode was measured for voltages less than the threshold voltage; two of the plots are shown in Fig. 3.9. These plots show that the behaviour is that of a double-tuned circuit and that the diode admittance plays an increasingly predominant role

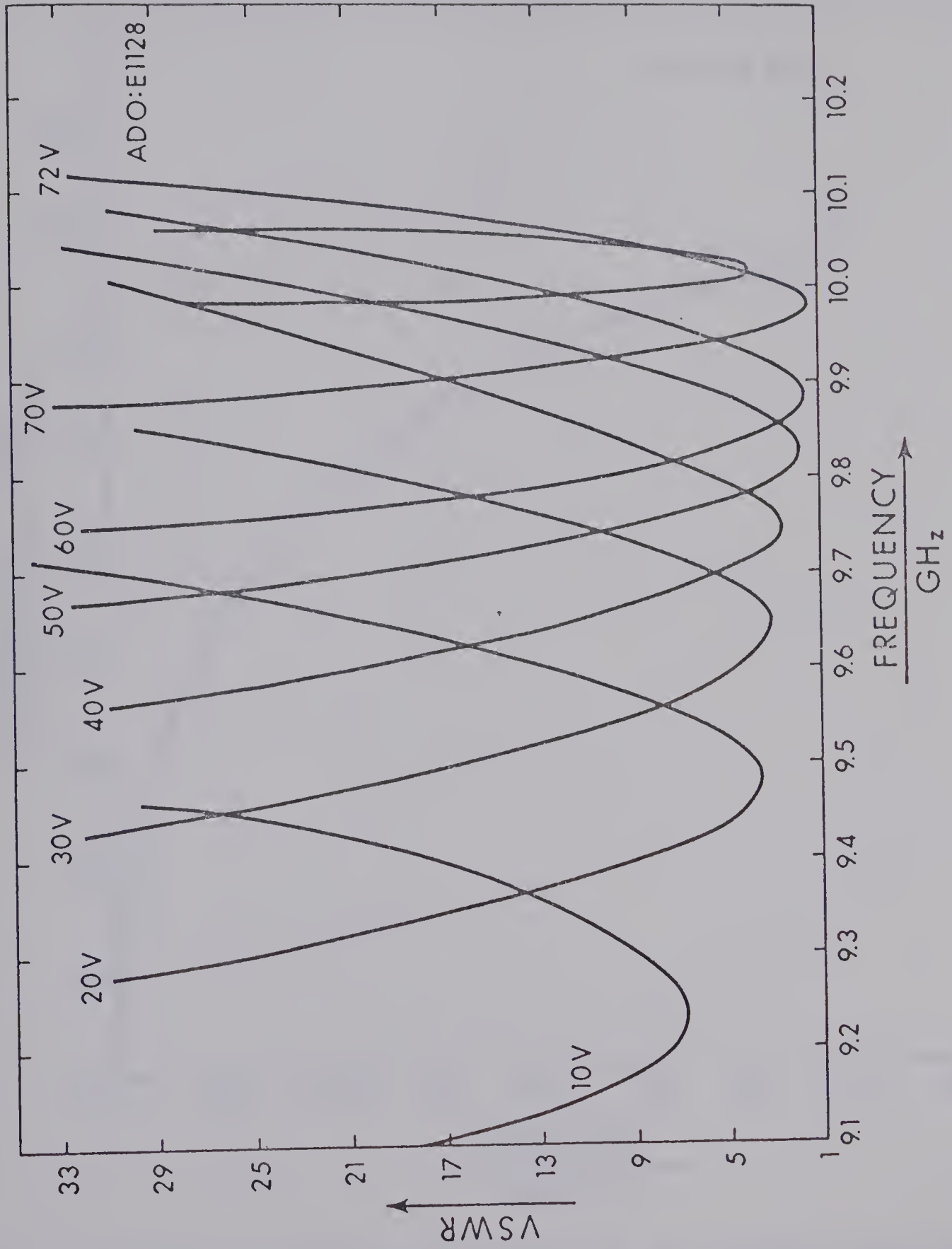


FIG. 3.7. VSWR VS FREQUENCY FOR DIFFERENT BIAS VOLTAGES

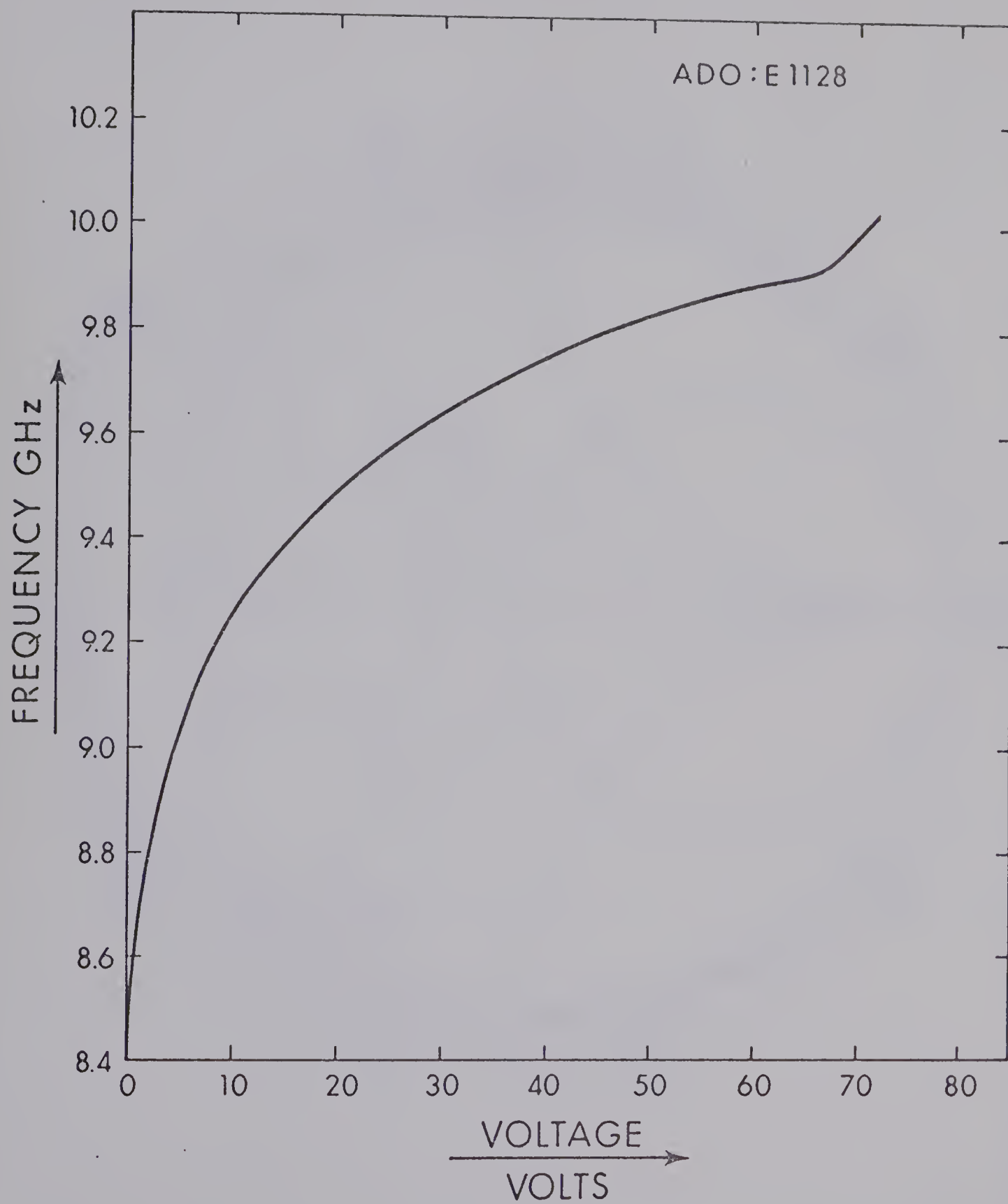


FIG. 3.8. RESONANT FREQUENCY VS BIAS VOLTAGE

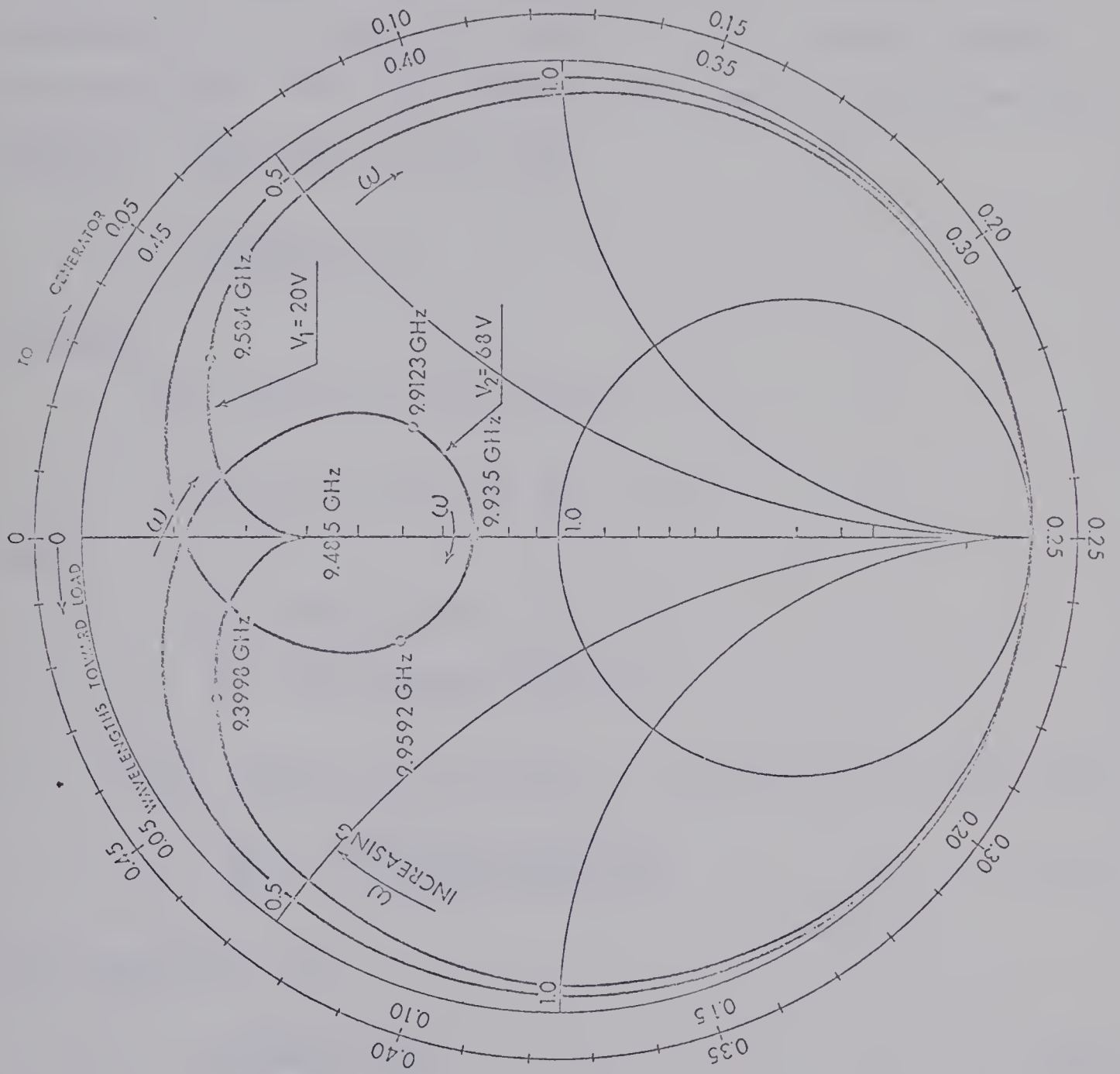


FIGURE 3.9. CIRCUIT ADMITTANCE FOR TWO BIAS VOLTAGES

with increasing bias voltage.

3.3 Procedure to Compute Electronic Admittance Below the Threshold Voltage

(1) From curves similar to Fig. 3.9, the normalised circuit conductance G_1 and normalised resistance R_1 at the resonant frequency point was noted. This conductance was with respect to the detuned-short position. Thus, (refer to Fig. 2.5)

$$(Z_{bb}/Z_0) = R_1$$

is known.

(2) From Figs. 3.10(a) and (b),

$$Y_{tot} = Y_e + Y_r \quad \text{and} \quad Z_{tot} = 1/Y_4$$

where

Y_e = the electronic admittance

Y_r = the resonator admittance.

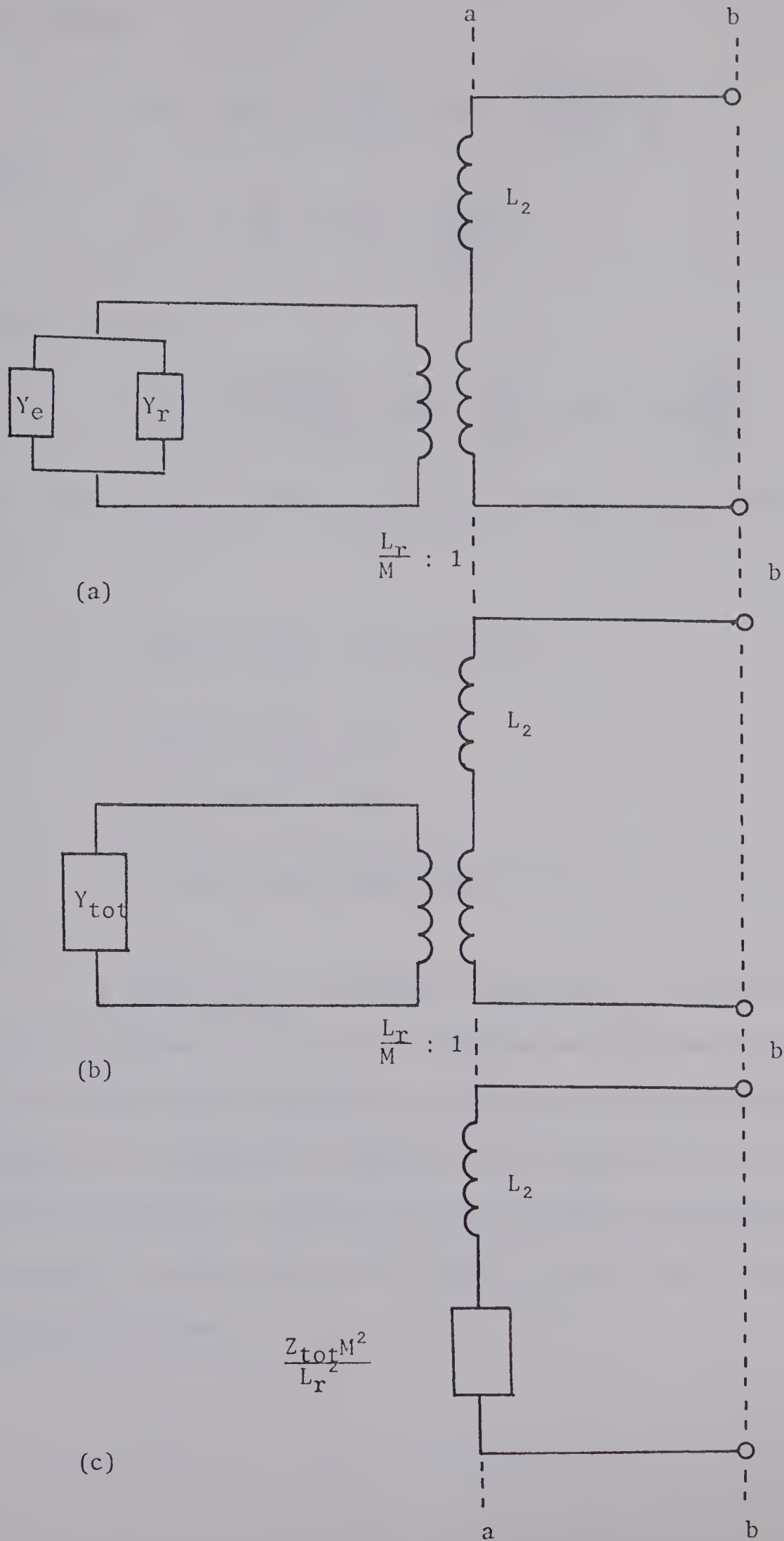
(3) (Z_{bb}/Z_0) was transformed to the plane of iris, which gave:

$$\frac{Z_{aa}}{Z_0} = \frac{(Z_{bb}/Z_0) + j \tan(-\beta \ell)}{1 + j (Z_{bb}/Z_0) \tan(-\beta \ell)} \quad \dots (3.3)$$

For convenience, let

$$\operatorname{Re} \left(\frac{Z_{aa}}{Z_0} \right) = (R2) \quad \dots (3.4)$$

$$\operatorname{Im} \left(\frac{Z_{aa}}{Z_0} \right) = (X2) \quad \dots (3.5)$$

FIG. 3.10. TRANSFORMATION OF Z_{tot} .

Then because $Z_0 = Z_{V,I}^{15}$:

$$Z_{V,I} \left[(R_2) + j(X_2) \right] = j\omega L_2 + \left(\frac{Z_{tot} M^2}{L_r^2} \right) \quad \dots (3.6)$$

where

$$Z_{V,I} = \frac{\pi b}{2a} \times 377 \left(1 - \frac{\lambda^2}{2a^2} \right)^{-\frac{1}{2}}.$$

From Eq. (3.6),

$$Z_{tot} = \left(\frac{L_r}{M} \right)^2 \left(Z_{V,I} (R_2) + j \left[Z_{V,I} (X_2) - \omega L_2 \right] \right) \quad \dots (3.7)$$

The values of ω , L_2 , (R_2) and (X_2) were known so Z_{tot} could be computed.

Then,

$$Y_{tot} = \frac{1}{Z_{tot}} = (G_{tot} + jB_{tot}) \quad \dots (3.8)$$

$$\text{Re } Y_{tot} = G_r + G_e \quad \dots (3.9)$$

$$\text{Im } Y_{tot} = B_r + B_e \quad \dots (3.10)$$

As G_r and B_r were both known, it was possible to compute G_e and B_e .

A graph of Y_{e1} , electronic admittance, in the pre-breakdown region, is shown in Fig. 3.11. The value of electronic conductance G_{e1} and electronic susceptance B_{e1} decrease with increasing bias voltage. The electronic conductance G_{e1} approaches zero near the breakdown voltage. The value of the electronic susceptance near breakdown is quite close to the value of large-signal susceptance obtained later on.

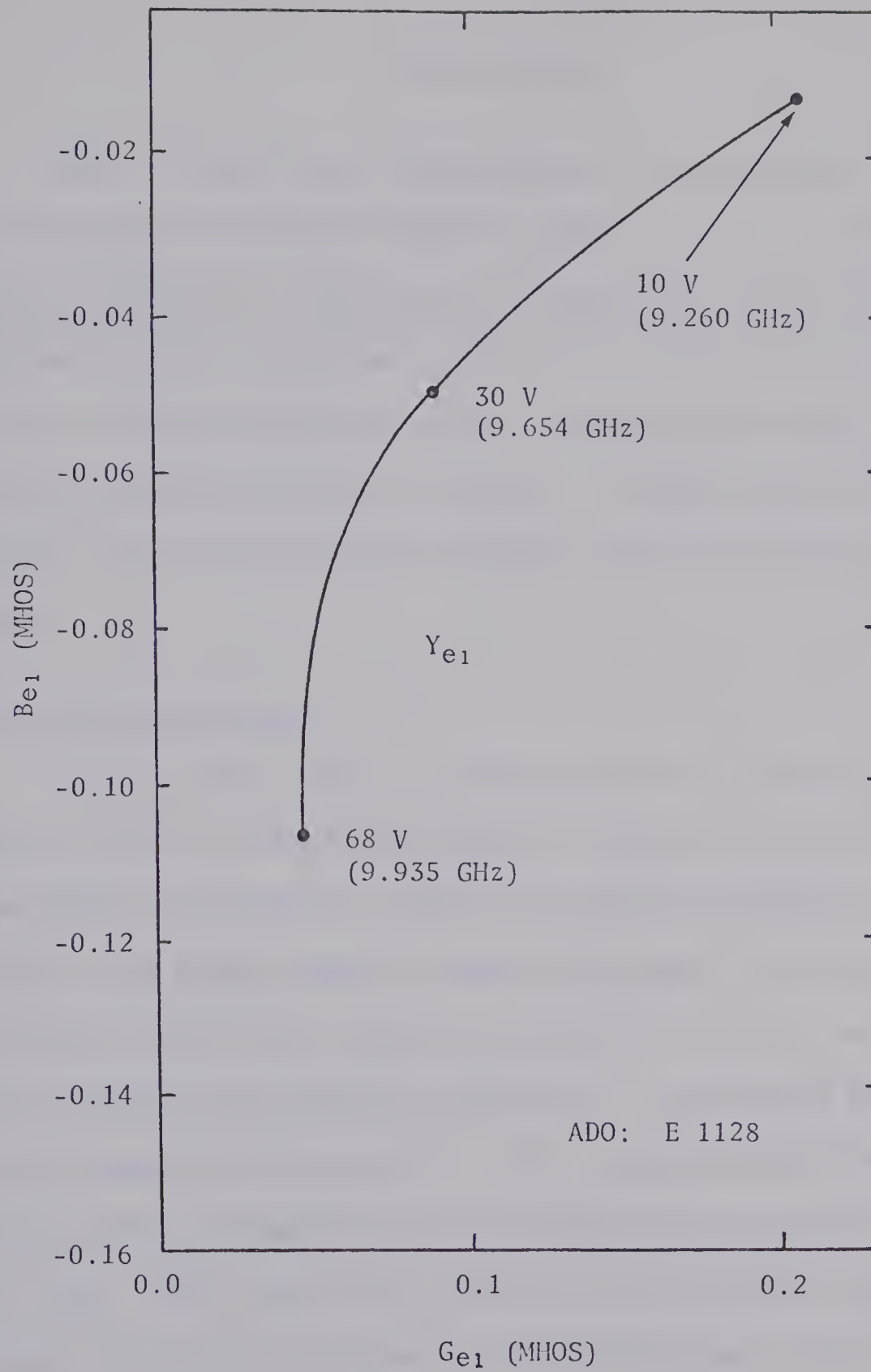


FIG. 3.11. SMALL-SIGNAL ELECTRONIC ADMITTANCE Y_{e1} vs BIAS VOLTAGE ($V < V_B$).

CHAPTER IV

RIEKE DIAGRAMS

Many microwave oscillators consist of an electronic current interacting with the fields within a resonant cavity. In solid-state microwave oscillators, semiconductor devices like IMPATT and Gunn diodes are generally housed in microwave cavities. The oscillator output is coupled to the load through an output transducer; the value of the load affects the operation of the oscillator. In this chapter, the theory of loading, which can be displayed graphically by Rieke diagram is studied.

4.1 The Oscillator Circuit^{17, 18}

An equivalent circuit representation of a microwave oscillator is shown in Fig. 2.1, where the parallel resonant circuits represent its various modes of operation. Because a microwave oscillator is designed to operate in a single mode for stable performance, the effect of all other modes, shown in the equivalent circuit of Fig. 2.1, will be minimal and may thus be normally neglected. The coupling transducer acts as an impedance transformer¹⁷. The load transformed through the transducer, with the impedance transforming characteristic $k_c (=L_r/M)$ is $k_c(G_\ell + jB_\ell)$. This then is the loading on the principal mode of the oscillator. By the use of these two simplifications, the circuit of Fig. 2.1 reduces to that of Fig. 4.1.

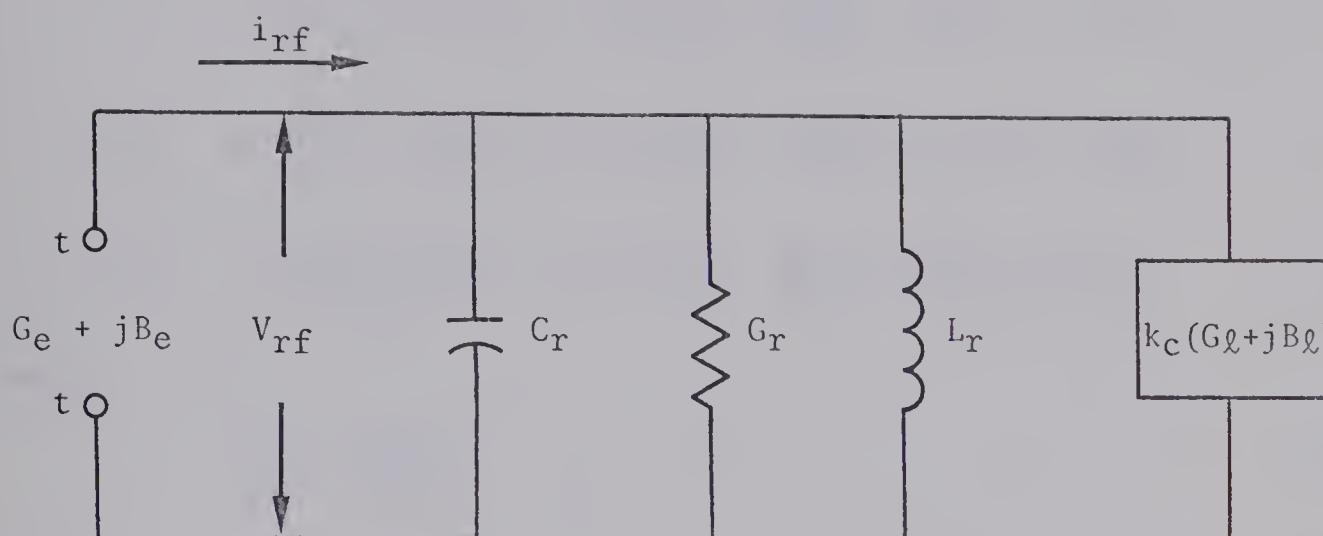


FIG. 4.1. SIMPLIFIED EQUIVALENT CIRCUIT OF OSCILLATOR.

4.2 Properties of a Self-Excited Oscillator as a Function of Load^{17, 19, 20}

If $(G_e + jB_e)$ is the electronic admittance at terminals t-t, then under equilibrium conditions, that is for steady state cw oscillations:

$$(G_e + jB_e) + G_r + j\left(\omega C_r - \frac{1}{\omega L_r}\right) + k_c(G_\ell + jB_\ell) = 0 \quad \dots(4.1)$$

$$\text{or} \quad -(G_e + jB_e) = G_r + j\left(\omega C_r - \frac{1}{\omega L_r}\right) + k_c(G_\ell + jB_\ell)$$

$$\text{or} \quad \frac{-(G_e + jB_e)}{\omega_o C_r} = \frac{1}{Q_o} + j\left(\frac{\omega}{\omega_o} - \frac{\omega_o}{\omega}\right) + k_c\left(\frac{G_\ell + jB_\ell}{\omega_o C_r}\right) \quad \dots(4.2)$$

where

$$\omega_o = \frac{1}{\sqrt{L_r C_r}} \quad \dots(4.3)$$

$$Q_o = \frac{\omega_o C_r}{G_r} \quad \dots(4.4)$$

and ω , is the angular frequency of oscillation.

Separating Eq. (4.2) into real and imaginary parts yields:

$$\frac{-G_e}{\omega_o C_r} = \frac{1}{Q_o} + \frac{k_c G_\ell}{\omega_o C_r} \quad \dots(4.5)$$

$$\frac{-B_e}{\omega_o C_r} \approx 2\left(\frac{\omega - \omega_o}{\omega_o}\right) + \frac{k_c B_\ell}{\omega_o C_r} \quad \dots(4.6)$$

The charge-carriers interact with the electromagnetic field within the resonator and transfer energy to them. One part of this energy helps maintain high fields in the resonator. Appreciable energy is stored in the cavity and as a result the cavity basically establishes the frequency of operation. However, the other part of the energy is fed through a coupling circuit to the load. The behaviour of the

oscillator can thus be expected to be affected by the load impedance.

Eq. (4.5) and (4.6) show the operational dependence of the oscillator upon the load. Eq. (4.5) shows that G_ℓ , the load conductance affects electronic conductance G_e , and consequently the rf voltage V_{rf} , the electronic power $P_{e\ell}$, and the circuit efficiency, and eventually the output power. The output power increases from zero to a maximum value and then decreases to zero again as G_ℓ increases from zero to infinity. That is, when $G_\ell = 0$, circuit efficiency vanishes although rf voltage developed would be high. At the other extreme $G_\ell = \infty$ and rf voltage falls to zero, thus the two nulls of power.

From Eq. (4.6)

$$2\left(\frac{\omega - \omega_0}{\omega_0}\right) = \frac{-B_e}{\omega_0 C_r} - \frac{k_c B_\ell}{\omega_0 C_r} \quad \dots(4.7)$$

Eq. (4.7) shows that, for a given G_ℓ , the frequency is determined by B_ℓ . The value of load conductance G_ℓ fixes B_e and from Eq.(4.7) this determines the frequency for a purely resistive load, i.e. when $B_\ell = 0$. The relative frequency deviation

$$\delta = \left(\frac{\omega - \omega_0}{\omega_0}\right) \quad \dots(4.8)$$

is inversely proportional to $(\omega_0 C_r / k_c)$ and is caused by changes in B_ℓ . The operating equations of an oscillator, as derived above, may be plotted as curves of constant power, and constant frequency, in an admittance plane, in which G_ℓ and B_ℓ are plotted as abscissa and ordinate, respectively. This information of power output and electronic tuning range as functions of load impedance is called the Rieke diagram. Ideally, constant power curves are lines parallel to the B_ℓ axis, and the constant frequency contours are all parallel to the curve

corresponding to $\omega = \omega_0$ and are vertically displaced from it. That particular contour is obtained by the simultaneous solution of the two equations

$$-\frac{G_e}{\omega_0 C_r} = \frac{1}{Q_0} + \frac{k_c G_\ell}{\omega_0 C_r} \quad \dots(4.9)$$

$$\text{and} \quad -\frac{B_e}{\omega_0 C_r} - \frac{k_c B_\ell}{\omega_0 C_r} = 0. \quad \dots(4.10)$$

As pointed out earlier, each value of G_ℓ yields a value of G_e ; this gives corresponding V_{rf} and subsequently B_e and B_ℓ . The above equations may be rewritten as:

$$G_\ell = -\left(\frac{\omega_0 C_r}{k_c}\right) \times \left(\frac{G_e}{\omega_0 C_r} + \frac{1}{Q_0}\right) \quad \dots(4.11)$$

$$\text{and} \quad B_\ell = -\left(\frac{B_e}{\omega_0 C_r}\right). \quad \dots(4.12)$$

These equations show that the curve of B_ℓ vs G_ℓ is similar to that of $-B_e$ vs $-G_e$, except for a change of scale given by the factor k_c and horizontal displacement given by the term $-\frac{\omega_0 C_r / k_c}{Q_0}$. In practice a sufficiently accurate approximation to this is a straight line which, in general, is not horizontal. The constant frequency curves are then a family of parallel straight lines which are not horizontal. The ideal Rieke diagram in the B_ℓ - G_ℓ plane is shown in Fig. 4.2.

If a transmission line of characteristic impedance Z_0 is terminated with a load impedance Z_L , the normalized impedance is

$$z = \frac{Z_L}{Z_0} = \frac{1}{(G_\ell + jB_\ell)} \quad \dots(4.13)$$

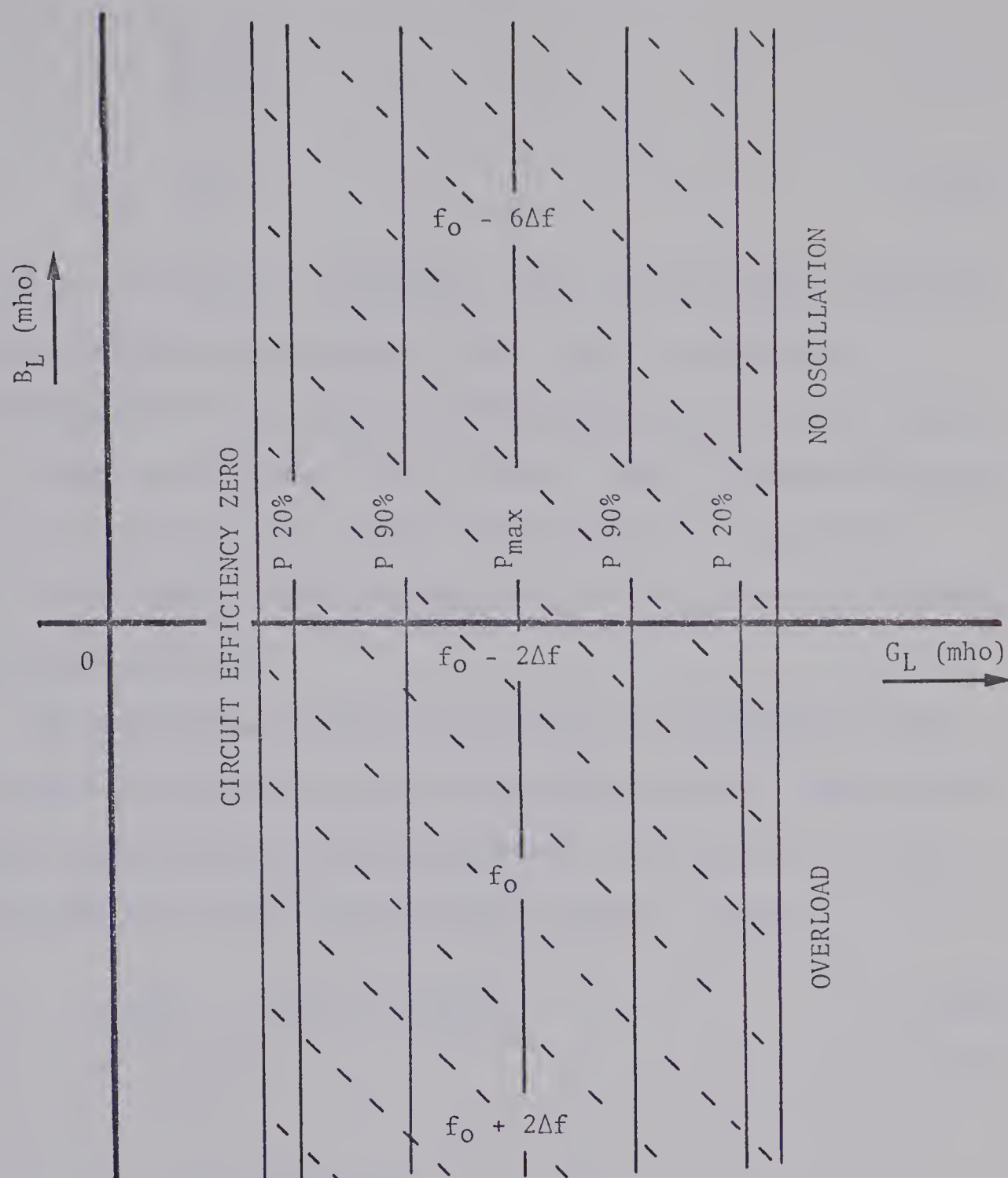


FIG. 4.2. IDEAL RIEKE DIAGRAM IN B - G PLANE.

Reflection coefficient, namely ρ is given by

$$\rho = \frac{Z_L - Z_0}{Z_L + Z_0} \quad \dots(4.14)$$

$$\text{or} \quad \rho = \frac{z - 1}{z + 1} \quad \dots(4.15)$$

Eq. (4.15) is a bilinear or fractional linear transformation expressing the relation between the variable ρ and z , and is a conformal transformation: that is, angles of intersection between ρ and z curves in the z -plane are preserved in the ρ -plane. Such a transformation also possesses the property that circles in the z -plane are mapped into circles in the ρ -plane, whereby circles of infinite radius are included, which are straight lines.

The contours of constant conductance and susceptance in the complex admittance plane are a set of orthogonal circles. Thus, in the reflection coefficient plane they represent a similar set, Fig. 4.3. Multiplication of Eq. (4.7) by the factor $\omega_0 C_r V_{rf}^2$, gives

$$-G_e V_{rf}^2 = G_r V_{rf}^2 + k_c G_\ell V_{rf}^2 \quad \dots(4.16)$$

$$\text{or} \quad P = P_D + P_0 \quad \dots(4.17)$$

where

P = power generated

P_D = power loss in cavity

P_0 = power output to load.

From Eq. (4.7) and $G_e = f(V_{rf})$ it is seen that for constant G_ℓ , both G_e and V_{rf} are also constant. Therefore constant G_ℓ implies constant power. Consequently, with the assumption that G_e is independent of frequency, constant-power contours will coincide with constant-

conductance curves of the Smith chart. As for any value of power less than maximum, there are two values of load conductance, the theoretical power curves are in general crescent shaped closed curves.

From Eq. (4.8), ω , the frequency of oscillation, is given by:

$$\omega = \frac{-B_e}{2C_r} + \omega_0 - \frac{k_c}{2C_r} B_\ell \quad \dots(4.18)$$

When G_ℓ , the load conductance is constant, and electronic susceptance B_e is independent of the frequency of oscillation, Eq. (4.18) is of the form:

$$\omega = k_0 - k_1 B_\ell \quad \dots(4.19)$$

where k_0 and k_1 are constants. Thus, each intersection of a constant frequency curve with a conductance circle leads to a unique value of B_ℓ . If the coefficients k_0 and k_1 are independent of G_ℓ , then the intersection on any G_ℓ circle would correspond to the same value of B_ℓ , thus, constant-frequency loci would coincide with constant-susceptance circles on the Smith chart. However, because the electronic susceptance B_e does change with the load conductance, the constant-frequency contours are distorted and diverge slightly from the B circles. The magnitude of the angle which constant frequency contours make with constant-susceptance circles is a function of the nonlinear electronic behaviour of the diode. All constant power curves ideally pass through the point of infinite admittance, in the reflection coefficient plane they will be circles tangent to the unit circle at the point of infinite admittance. The constant frequency curves pass through this point also but, at a different angle. The ideal Rieke diagram in circle-diagram-form is shown in Fig. 4.3 for the same oscillator as

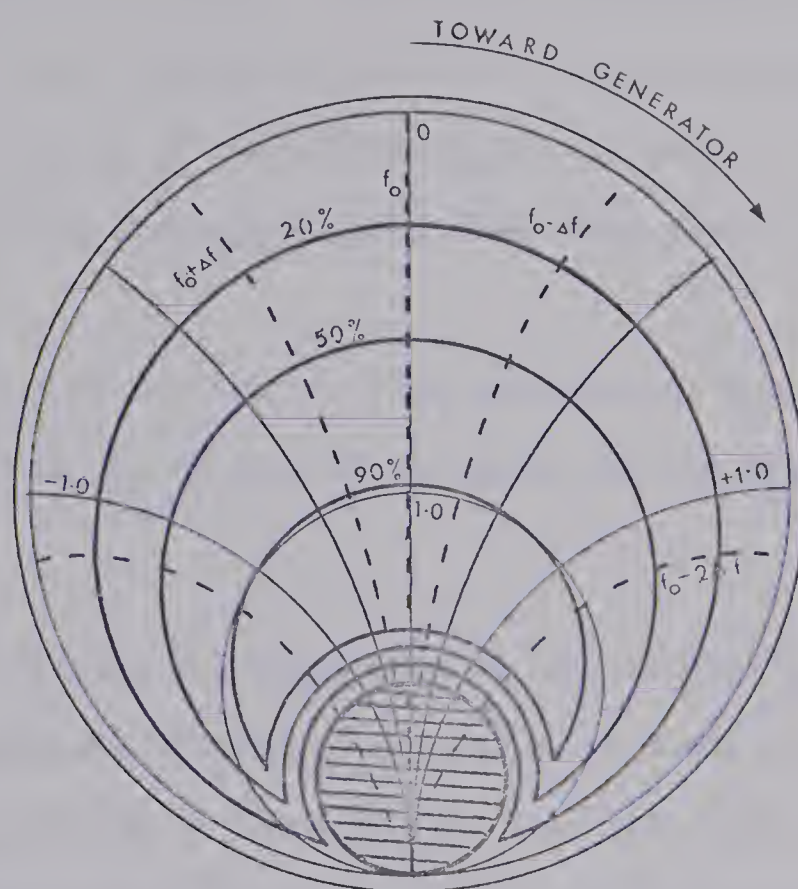


FIG. 4.3. IDEAL RIEKE DIAGRAM IN CIRCLE-DIAGRAM FORM
FOR THE SAME OSCILLATOR AS IN FIG. 4.2.

used for Fig. 4.2. This diagram is derived on the assumption that the load is located at the plane of the detuned-short in the output line. The plane of the detuned-short is a function of frequency and is an integral number of half-wavelengths from the resonator. If the Rieke diagram is taken across a fixed plane at a point beyond the device terminals, the constant frequency curves will depart even further from the constant-susceptance circles. The angle through which any curve is rotated depends on the different electrical distances of the plane of reference from the plane of the detuned-short, as shown in Fig. 4.4. The result is that the frequency curves cross near a point inside the unit circle.

Rieke diagrams constructed from experimental data depart from the ideal form due to one or more of the above and the following reasons:

- (1) The varying reactance coupled into the oscillator may affect the electronic properties of diode by distorting the pattern of electric fields in the cavity and these effects may give rise to kidney-shaped curves.
- (2) The measurement of power is likely to be in error, as the standing wave ratio increases, particularly if the power lost in the standing wave detector or reflectometer is not taken into account.
- (3) If the lead used in the experiment is resonant, some of the regions of Rieke diagram cannot be explored. This is because the load is a rapidly varying function of frequency and the stability conditions are critical.

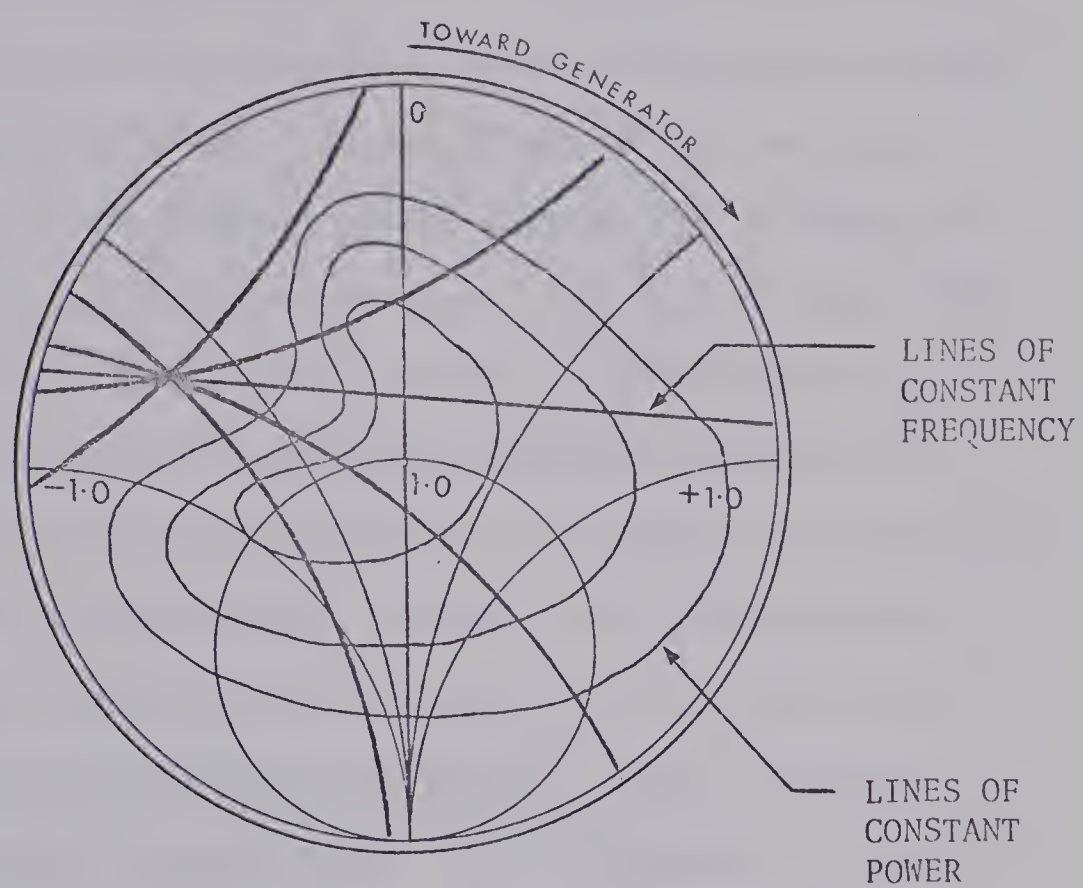


FIG. 4.4. ACTUAL RIEKE DIAGRAM.

CHAPTER V

REFLECTOMETER BRIDGE SET-UP,

DETERMINATION OF RIEKE DIAGRAM

AND OF ELECTRONIC ADMITTANCE

A reflectometer arrangement was employed for the measurement of load admittance, as shown in Fig. 5.1. Initially, a slotted-line technique was used for the measurements, but this method was discarded due to difficulties posed by the high sensitivity of the oscillator power and frequency to the movement of the slotted line carriage and by the difficulty of accurately measuring very low and very high VSWR's in this way. Moreover, with a slotted line it is necessary to use a sensitive galvanometer as the indicator of VSWR (if no modulation is used). Even a small drift in the zero of the instrument would introduce a large error in the computed VSWR. The effect of source amplitude instability, which is serious when a slotted section is used, has been eliminated by a closed-loop measuring technique. Also, the source mismatch which can cause serious errors in the measurement of very low values of VSWR with a slotted line is not nearly as critical in reflectometer measurements.

5.1 The Reflectometer Bridge

The reflectometer arrangement may be employed for the measurement of an unknown load in general and the load presented to an oscillator in particular. The reflectometer arrangement used for the measurement of electronic admittance is shown in Fig. 5.1. In this

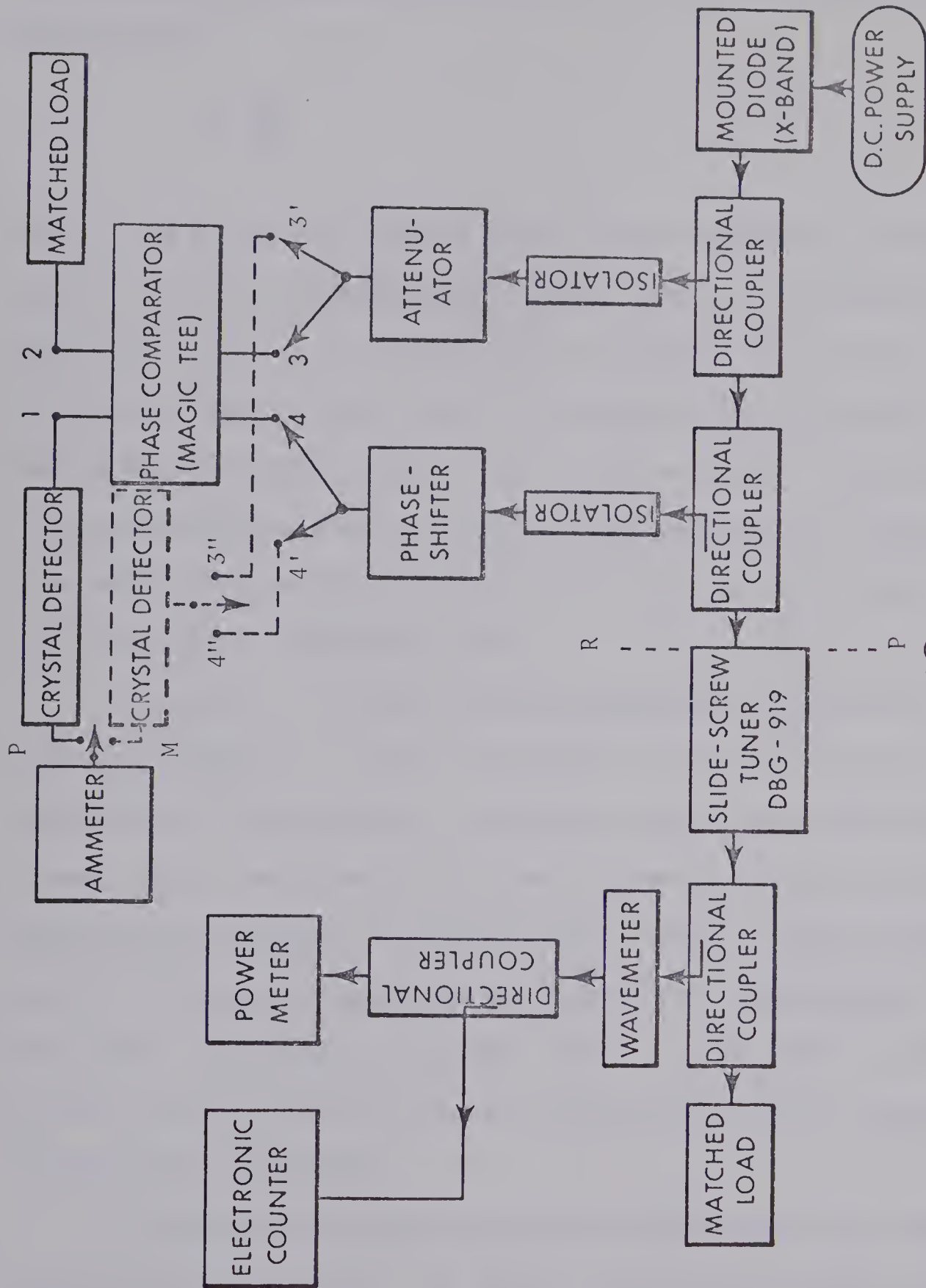


FIG. 5.1.

REFLECTOMETER BRIDGE SET-UP FOR DETERMINING THE EFFECT
OF LOAD ADMITTANCE ON OSCILLATOR BEHAVIOUR

set-up, samples of incident and reflected waves are taken and compared, yielding both the magnitude and the phase of reflection coefficient. Mathematically,

$$\bar{\rho} = \frac{\bar{E}_r}{\bar{E}_i} \quad \dots(5.1)$$

where \bar{E}_i and \bar{E}_r are the electric field vectors associated with the incident and reflected waves from the load, and $\bar{\rho}$ is the reflection coefficient. That is, $\bar{\rho}$ at a particular reference plane can be determined by obtaining the ratio of the amplitudes of \bar{E}_i and \bar{E}_r and the phase-difference between them at that reference plane. The microwave bridge reflectometer shown in Fig. 5.1 makes possible the evaluation of $\bar{\rho}$, at reference plane RP, by giving a measurable relation between E_i and E_r , and the phase angle between them.

In Fig. 5.2 is shown a simple reflectometer, using two directional couplers to sample the incident and reflected wave, respectively. Alternatively, a single dual-directional coupler could be used. Also, two detectors of known response law with accompanying amplifiers are required. To calibrate this set-up, a short-circuit is placed at the load terminals and the amplifiers are adjusted for equal indications. To measure the unknown load, it is connected in place of the short, then the ratio of the two indications gives the magnitude of the reflection coefficient.

The above method does not give any information about phase of the reflection coefficient. By certain circuit modifications, however, it is possible to obtain this information also. One method of getting the phase-information is to form a closed loop in the incident and reflected signal channels and include a hybrid ring or a magic-T in it.

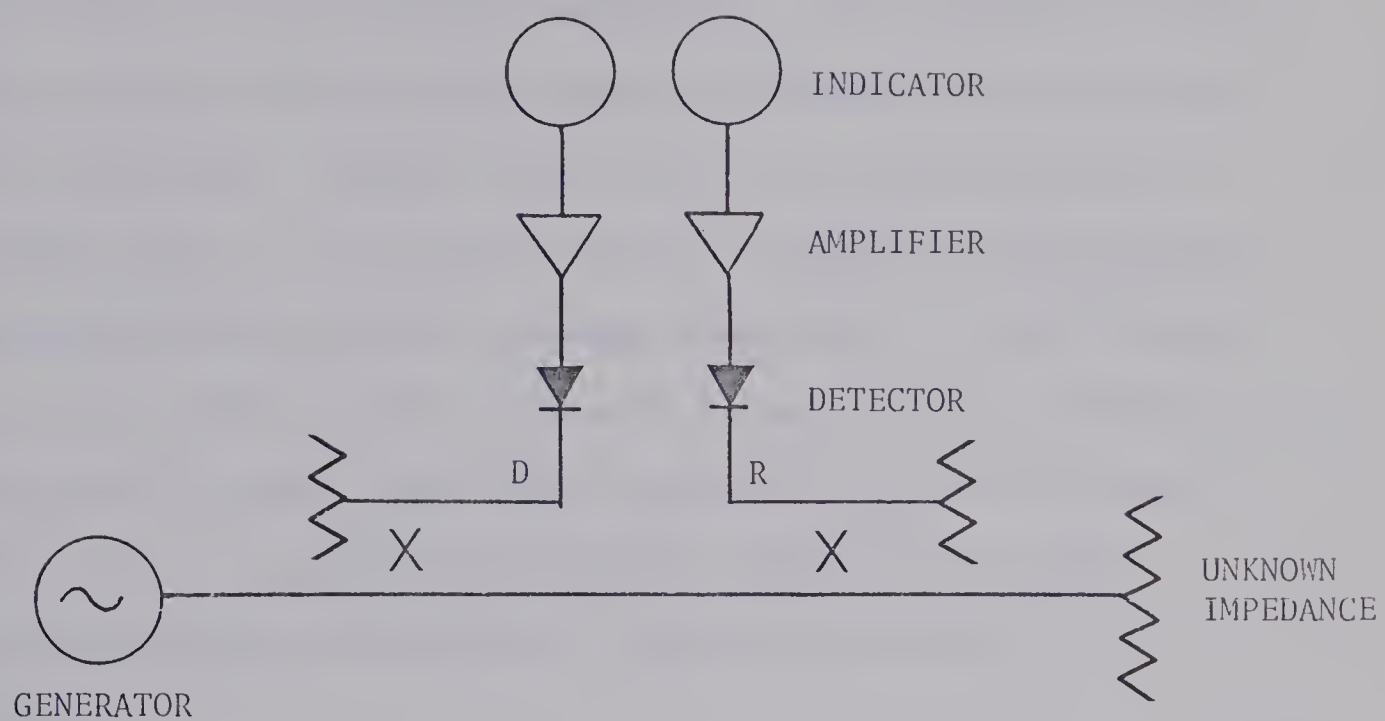


FIG. 5.2. THE MICROWAVE REFLECTOMETER. D AND R ARE DIRECTIONAL COUPLERS TO SAMPLE INCIDENT AND REFLECTED WAVES, RESPECTIVELY.

One simple set-up is shown in Fig. 5.3²¹. Here, one arm of the hybrid ring gives the sum of the incident and reflected wave signals, and the other their difference. Thus, the phase shifter needs to have a range of only 180° to obtain minimum indication. The incident and reflected signals are sampled by arms 3 and 4. The phase-shifter and attenuator are adjusted to give minimum detector output. The measured attenuation is proportional to the reflection coefficient. It is possible to obtain the phase information because the signals are compared before the phase is lost in detection. The main source of error is the variation of signal phase-shift in arm 3 and of signal attenuation in arm 4 produced by attenuator and phase-shifter settings respectively. Also, the noise-level is a limitation when the unknown is a nearly matched termination. Another source of error is the finite directivity of the directional couplers, but it is possible to incorporate compensation whereby imperfect performance of directional couplers can be partly eliminated^{21, 22}.

However, for the actual measurement set-up (Fig. 5.1) the arrangement of Fig. 5.3 was modified to include two directional couplers that help isolate the reverse and forward signals. In addition, the circuit elements were arranged such that the phase and attenuation measurements could be made independently. The magnitude of reflection coefficient was obtained by the comparison of reflected voltage with incident voltage, quantities which are generally of dissimilar magnitude. The reflectometer arrangement of Fig. 5.3, on the other hand, compares (incident voltage + reflected voltage) with (incident voltage - reflected voltage) which, for small reflections, are comparable in magnitude.

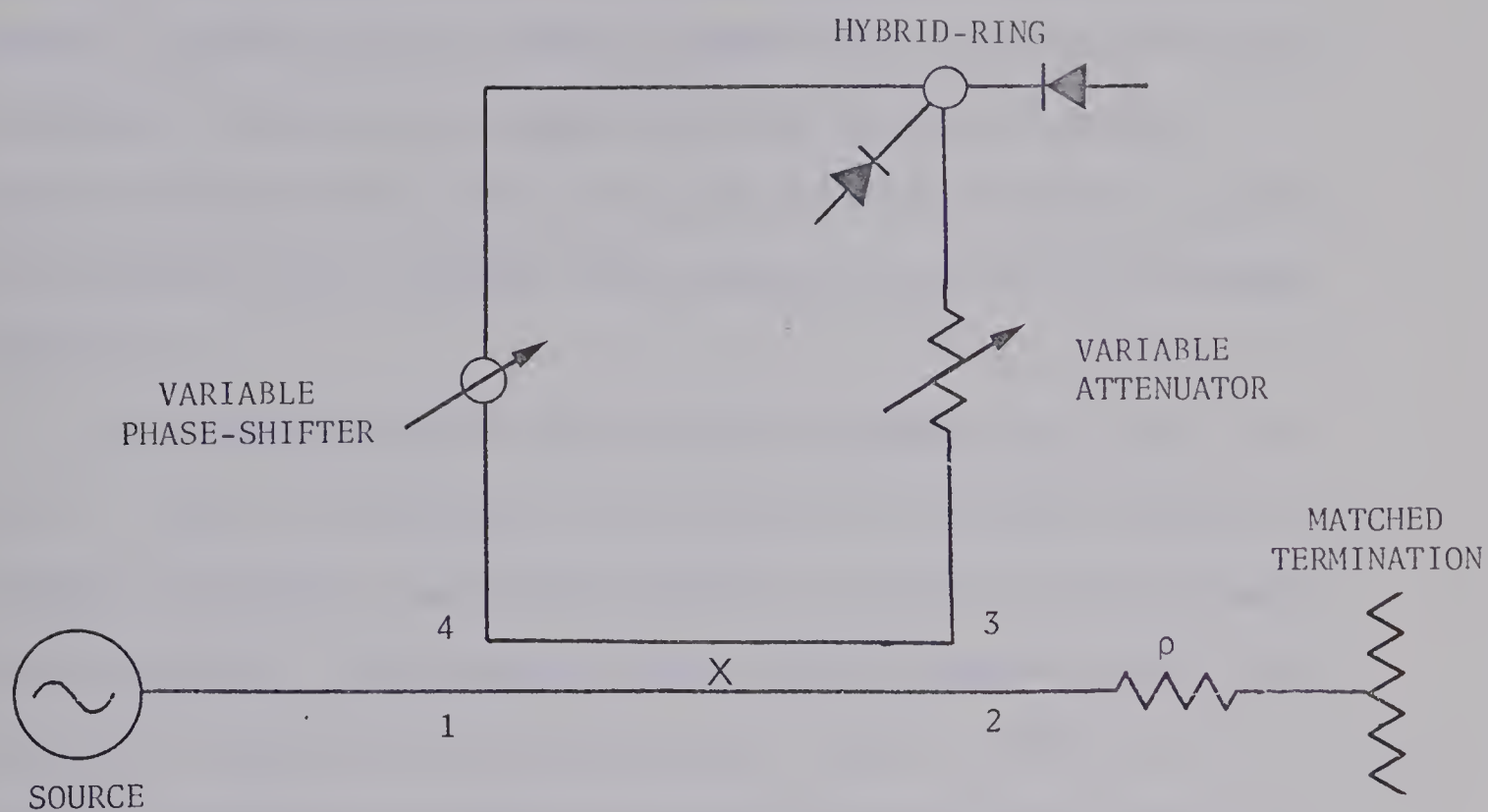


FIG. 5.3. REFLECTOMETER ARRANGEMENT WITH HYBRID-RING.

5.2 Measurement Circuit Used

In the circuit used for measurement of load impedance (Fig. 5.1), two 10dB directional couplers of directivity greater than 40dB were attached to the oscillator output, one in the forward, and the other in the reverse direction. The sampling ports were connected to isolators (minimum isolation 30dB) to enhance the isolation of the main transmission line from the "comparison" and "detection" systems. A precision attenuator (hp X382A) and a precision phase-shifter (hp X885A) were connected in the incident and reflected signal arms of the bridge, respectively.

The sampled signals were fed into conjugate arms 3 and 4 of a magic-T. Port 1 of the magic-T was connected to a detector and port 2 to a matched termination. Power fed from port 3 or port 4 divides equally into arms 1 and 2. The reflected signal from the unknown load is fed into port 4, one half of the energy going to port 2, where it is completely absorbed by a matched load, the other half going into arm 1, where it combines with half of the incident signal applied to port 3. If the phase-shifter preceding the input to arm 4 is adjusted to bring the signal samples into phase-opposition, the indicator connected to the output detector will show a minimum. Thus, after appropriate calibration of this set-up, the phase-information can be extracted.

This arrangement makes the determination of the phase-angle of the reflection coefficient independent of the characteristics of the crystal detector.

To find ρ , the magnitude of reflection coefficient, the incident wave sample and the reflected wave sample are compared. The reflected wave is channelled to 4' and thence to a crystal detector (switched to

4"), whose output is connected to a micro-ammeter (switched to position M); the indication is noted. Then switch positions are changed such that the incident wave via attenuator, 3', 3" and crystal detector also goes to the micro-ammeter (switched to position M). The precision attenuator is adjusted to give the same indication on the micro-ammeter as that already obtained for the reflected wave. In the calibration procedure that follows, it is shown how the above readings were used to compute ρ and ϕ , where the reflection coefficient is $\bar{\rho} = \rho e^{j\phi}$. Again the crystal detector is only used to compare the two signals and its absolute response is of no great consequence, i.e. the deviations from the square law response do not significantly effect the results.

The main transmission line of the reflectometer bridge was connected to a matched termination which was preceded by a slide-screw tuner (DBG-919), by means of which the magnitude and phase angle of the impedance seen by the oscillator could be varied. The power dissipated in the matched termination and the frequency of the signal were determined by sampling the signal through a directional coupler. The sampled signal was split to feed a power meter and an electronic counter. A wavemeter was used to check the frequencies for the case where the generator gave, simultaneously, multiple frequencies instead of a single frequency.

5.3 Calibration and Testing of Reflectometer Bridge

A microwave reflectometer bridge technique was employed to measure the load admittance presented to the oscillator. First, it is necessary to calibrate the bridge set-up. After calibration, the impedance was readily obtained by plotting the obtained data on a Smith chart. The measurement accuracy is primarily dependent upon the

properties of the components used in the construction of the bridge circuit; it is independent of signal-level and of detector response law.

Impedance measurements at low frequencies are made by comparison of the unknown impedance against a standard impedance. At low rf, suitable impedance standards can be readily designed; however, with increasing frequency, this becomes more and more difficult; accurate microwave impedance standards are not readily available. Pure reactive loads can be simulated by appropriate lengths of uniform lossless transmission lines. The reflectometer bridge was calibrated by utilizing a short circuit and a standard reflection $\rho = 0.2$ (hp X916E). The bridge was tested by measuring impedance $(1 + jX)$, made by connecting a variable shorting stub in series with the matched termination Z_0 . The impedance actually used was a series "T" waveguide junction with a matched load at one port and a movable short at the other port, Fig. 5.4.

The reactive component of this impedance is a function of the length of the shorting stub. Thus the normalised impedance gives the expression $(1 + jX)$ with change of position of the short. Actually, due to discontinuities in the waveguide T junction, there are junction reactances which are frequency dependent.

To calibrate the microwave bridge reflectometer, a short (Sanders, Model 16/2) was connected at the reference plane RP (Fig. 5.1) and the reading of the phase-shifter noted. A reading of -19° was obtained, (ideal reading -180°). Thus to the phase-shifter readings, -161° has to be added to correct for unequal incident and reflected signal paths in the measuring circuit.

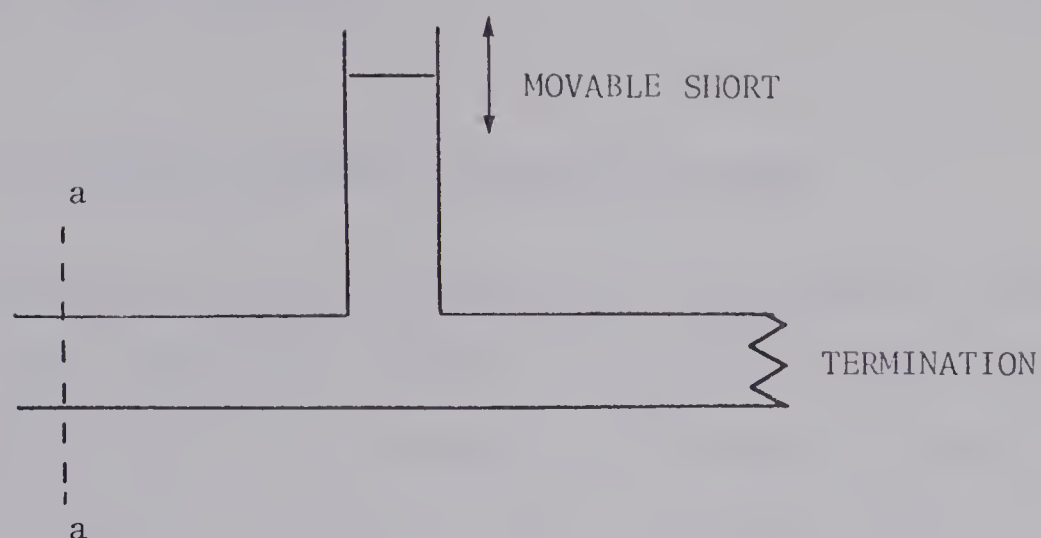


FIG. 5.4. WAVEGUIDE "T" JUNCTION TERMINATED WITH ITS CHARACTERISTIC IMPEDANCE AND A MOVABLE SHORT IN THE TWO ARMS.

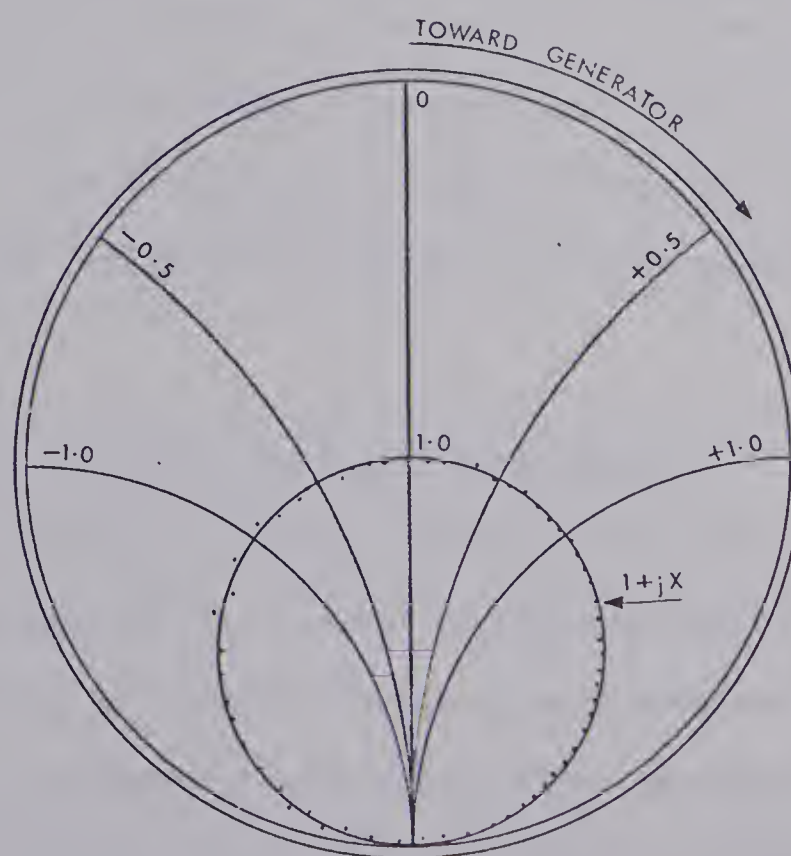


FIG. 5.5. PLOT OF IMPEDANCE VARIATION WITH MOVEMENT OF SHORT, FOR THE WAVEGUIDE CIRCUIT OF FIG. 5.4.

The magnitude of the reflection coefficient ρ , was computed by use of the equation:

$$(d - 3.01) = 20 \log \frac{1}{\rho} \quad \dots(5.2)$$

where

d = attenuator reading to balance the bridge.

The correction for excess attenuation in the reflected signal path is 3.01dB. This factor was obtained by balancing the bridge with a standard reflection of $\rho = 0.2$ connected at the reference plane RP, Fig. 5.1. The attenuator reading was 17.0dB. To obtain a VSWR of 1.5 ($\rho = 0.2$), it was found from Eq. (5.2) that 3.01dB has to be subtracted from the attenuator reading. This gives the constant 3.01dB in Eq. (5.2).

To test the above measurement set-up, the impedance $(1 + jX)$ of Fig. 5.4 was measured at 10.0 GHz. The reactive part was changed by varying the position of the short. The results, after adjustments, are shown in Fig. 5.5. The data points lie fairly close to the $(1 + jX)$ circle, so this plot reflects the accuracy of the microwave reflectometer bridge.

5.4 Rieke Diagram and Circuit Admittance Measurements

To obtain the Rieke diagram, load impedances and oscillator power levels were measured for a series of operating points at several frequencies. Contours of constant frequency were obtained by plotting these data; then, by interpolation between points corresponding to different powers on these constant frequency curves, contours of constant power were obtained. For example, to plot a curve of constant frequency

f_1 , the load was first adjusted so that the oscillator operated at frequency f_1 then the ϕ and dB readings were noted. Next, the slide-screw tuner position was changed slightly, thus perturbing the frequency; the frequency of the oscillator signal was brought back to f_1 by adjusting the slide-screw penetration. This procedure was repeated until sufficient data at that frequency had been obtained. Other constant frequency curves were obtained in a similar manner. The data included readings of load power, frequency, phase-shifter and attenuator settings. The constant power contours were obtained by interpolation, and smooth curves were drawn through the points. The Rieke diagram at the plane of the iris was obtained for ADO: E1128 and is shown in Fig. 5.6.

The constant frequency curves are skew; the reason for their departure from constant susceptance is that the electronic susceptance is not independent of power. The constant power curves are not closed; however, they do form a nested set. Stability conditions near the region, marked "sink" are critical. Close to this region, multiple frequencies can develop, while frequency jumps and irregularity in frequency shift with change of load can occur.

Sample Calculation of ϕ ; Phase Angle of Reflection Coefficient

Suppose a minimum ammeter reading is obtained when the phase-shifter is set to $\phi_m = 301.5^\circ$. Then, uncorrected phase is

$$\phi_{uc} = -\phi_m = -301.5^\circ \quad \dots(5.3)$$

The bridge was calibrated at 10.00 GHz, the angle correction here was -161° . Therefore, at frequency f_s , the angle correction would be,

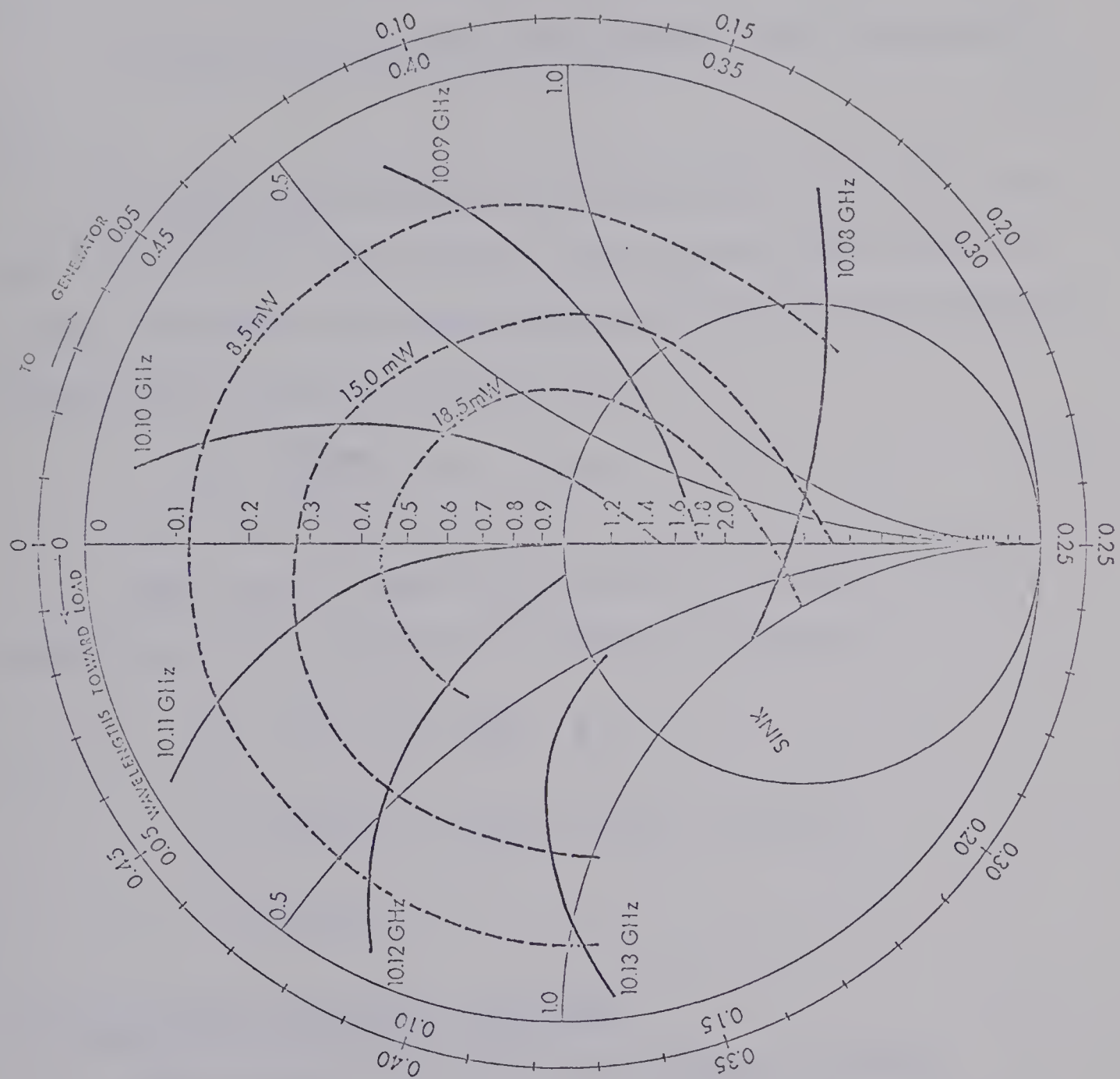


FIGURE 5.6. RIEKE DIAGRAM OF THE OSCILLATOR

$$\phi_1 = \left(\frac{-161 \times \lambda_{g1}}{\lambda_{gs}} \right) = -161.5 \quad \dots(5.4)$$

where

λ_{g1} = guide wavelength at 10.00 GHz

λ_{gs} = guide wavelength at f_s GHz.

To convert the impedance into admittance, 180^0 were added to ϕ_{uc}(5.5)

The load admittance has to be transformed to the plane of the iris. The distance of the reference plane from the plane of the iris is equal to 84.33 cm. The angle through which the point must rotate on the Smith chart toward the generator is ϕ_2 :

$$\phi_2 = \left(\frac{84.33}{\lambda_{gs}} \right) \times 720^0 = 223.0^0 \quad \dots(5.6)$$

Thus, the true angle for admittance at the plane of the iris, by use of Eq. (5.3) through (5.6), called ϕ_c is given by:

$$\begin{aligned} \phi_c &= (-\phi_m + \phi_1 + 180^0 - \phi_2) \\ &= (-301.5^0 - 161.5^0 + 180.0^0 - 223.0^0) \\ &= 214.0^0 \end{aligned}$$

5.5 Calculation of Electronic Admittance

The electronic admittance was calculated as follows:

(1) Values of normalised load admittance (Y_L/Y_O), at the plane of the iris (a-a), (Fig. 2.5) were read from the Rieke diagram. These values were then converted into impedance (Z_L/Z_O) = (Y_O/Y_L).

(2) The value of Z_L was obtained by multiplying (Z_L/Z_0) by the characteristic impedance of the waveguide defined on a voltage-current basis¹⁵.

$$\therefore Z_L = (Z_L/Z_0) \times Z_{V,I}$$

where

$$Z_{V,I} = \frac{\pi}{2} \times \frac{b}{a} \times 377 \times \left(1 - \frac{\lambda^2}{4a^2}\right)^{-\frac{1}{2}}$$

where a and b are the broad and narrow inside dimensions of the waveguide, respectively.

(3) A reactance $Z_2 (= \omega L_2)$ was added to each value of load impedance Z_L . That is,

$$Z_{\text{sum}} = (Z_L + Z_2).$$

(4) This sum impedance Z_{sum} , when transformed through the ideal transformer is:

$$Z_C = \left(\frac{L_R}{M}\right)^2 \times Z_{\text{sum}} \quad \dots(5.7)$$

hence

$$Y_C = \frac{1}{Z_C} \quad \dots(5.8)$$

The resonator impedance Y_R is

$$Y_R = G_R + j\left(\omega C_R - \frac{1}{\omega L_R}\right). \quad \dots(5.9)$$

Then, total circuit admittance seen by the diode is,

$$Y_{\text{total}} = Y_R + Y_C. \quad \dots(5.10)$$

As the diode was in cw operation when the Rieke diagram was obtained, it must satisfy the criteria for steady-state oscillation:

$$Y_{e2} + Y_R + Y_C = 0$$

or $Y_{e2} = -(Y_R + Y_C) = -Y_{\text{total}} \quad \dots(5.11)$

Values of electronic admittance Y_{e2} so obtained are plotted in the admittance plane, Fig. 5.7. Some of the power points are marked-off on these curves.

The skew nature of the constant frequency curves is carried over to the electronic admittance plots. The output power of the oscillator increases with increasing negative electronic conductance.

5.6 Hysteresis Phenomena

When a controlling parameter of the oscillator was varied, such as bias current or load impedance, it was found possible to obtain conditions where the frequency would jump from one value to another; furthermore, if the direction of change of the controlling parameter was reversed, the frequency jump would occur between two frequencies different from those between which the jump occurred earlier. Before these frequency jumps occurred, several sidebands, spaced close to the main signal, would appear and the frequency jump would occur to the stronger of these parasitic components. It was found that this condition can occur if the circuit is such that the circuit admittance versus frequency curve as seen by the diode has multiple intersections with the electronic admittance curve, as shown by Kurokawa²³. Varying a controlling parameter of the oscillator changes the shape and position of these curves, and hence moves their points of intersections or causes points of intersection to be eliminated or created. When the

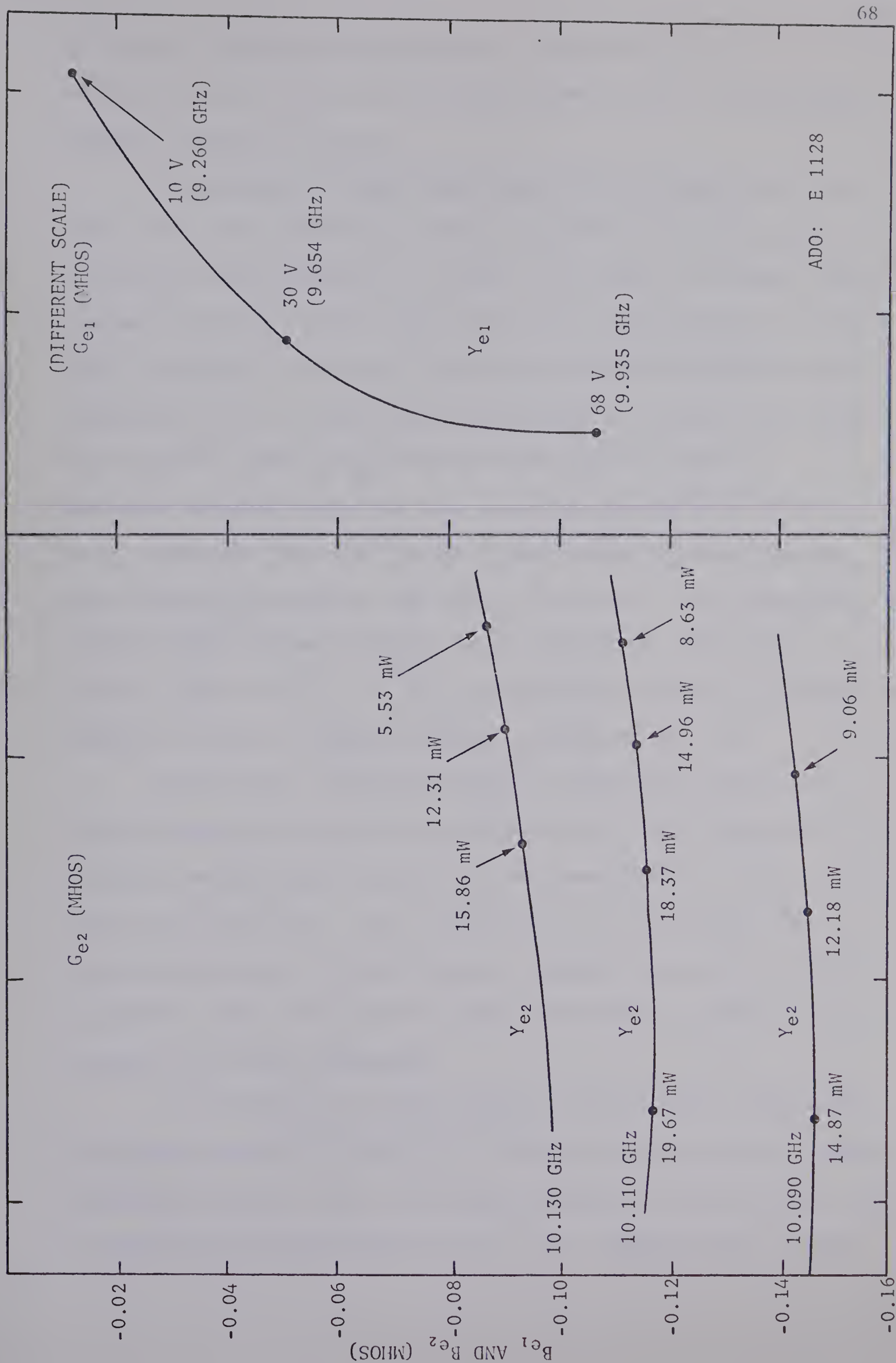


FIG. 5.7. SMALL-SIGNAL ELECTRONIC ADMITTANCE Y_{e1} VS BIAS VOLTAGE ($V < V_B$),

ELECTRONIC ADMITTANCE Y_{e2} VS OUTPUT POWER FOR CONSTANT FREQUENCIES.

oscillator's operating point occurs at a particular point of intersection that ceases to be a stable operating point, discontinuous frequency changes will occur.

The hysteresis effect with varying load is shown in Fig. 5.8. These curves were obtained by varying the slide-screw tuner position at a constant screw penetration. For small screw depths, the power versus frequency curves are closed whereas, for larger penetrations, they are open. For example, for curve V, when the slide-screw tuner was moved towards the load, the power varied and frequency decreased until point A'' was reached, whence the operating point jumped to point B''. Continuous movement toward the load caused the portion B''-A''-B''-A''... to be continuously retraced. However, when the slide-screw tuner was moved towards the generator, the curve C''-D''-C''-D''... was traced out. Similar results were obtained for curves III and IV. Before the frequency jump from A, A', C, etc. occurred, many frequency components appeared; a typical frequency spectrum is shown in Fig. 5.9.

When another controlling parameter, the diode current, was varied, frequency hysteresis was again observed. This irregularity in frequency variation with current is again present only for large reflection coefficients. Fig. 5.10 and Fig. 5.11, illustrate the hysteresis phenomenon. Extra frequency components appeared at point A and point C; there the output was noisy and the jump occurred to the stronger of the extra components.

To investigate the load conditions when frequency jumps occur, the circuit admittance across Y_c , as a function of frequency was computed and plotted (see Fig. 5.12). The applicable part of the admittance curve is reproduced in enlarged form in Fig. 5.13. Comparing Fig. 5.13 and

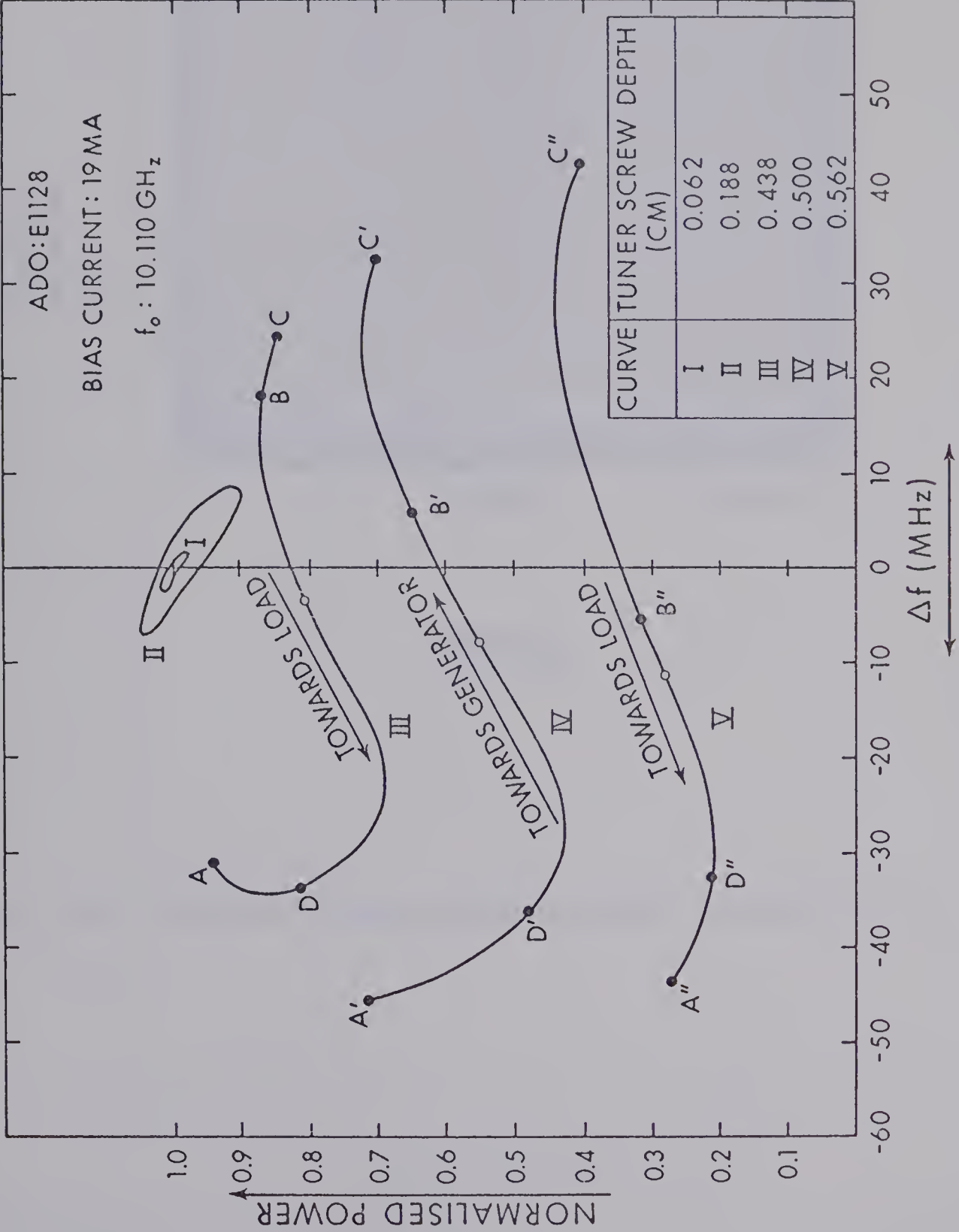


FIG. 5.8. CHANGE OF LOAD POWER AND FREQUENCY
AS A FUNCTION OF SLIDE SCREW TUNER POSITION

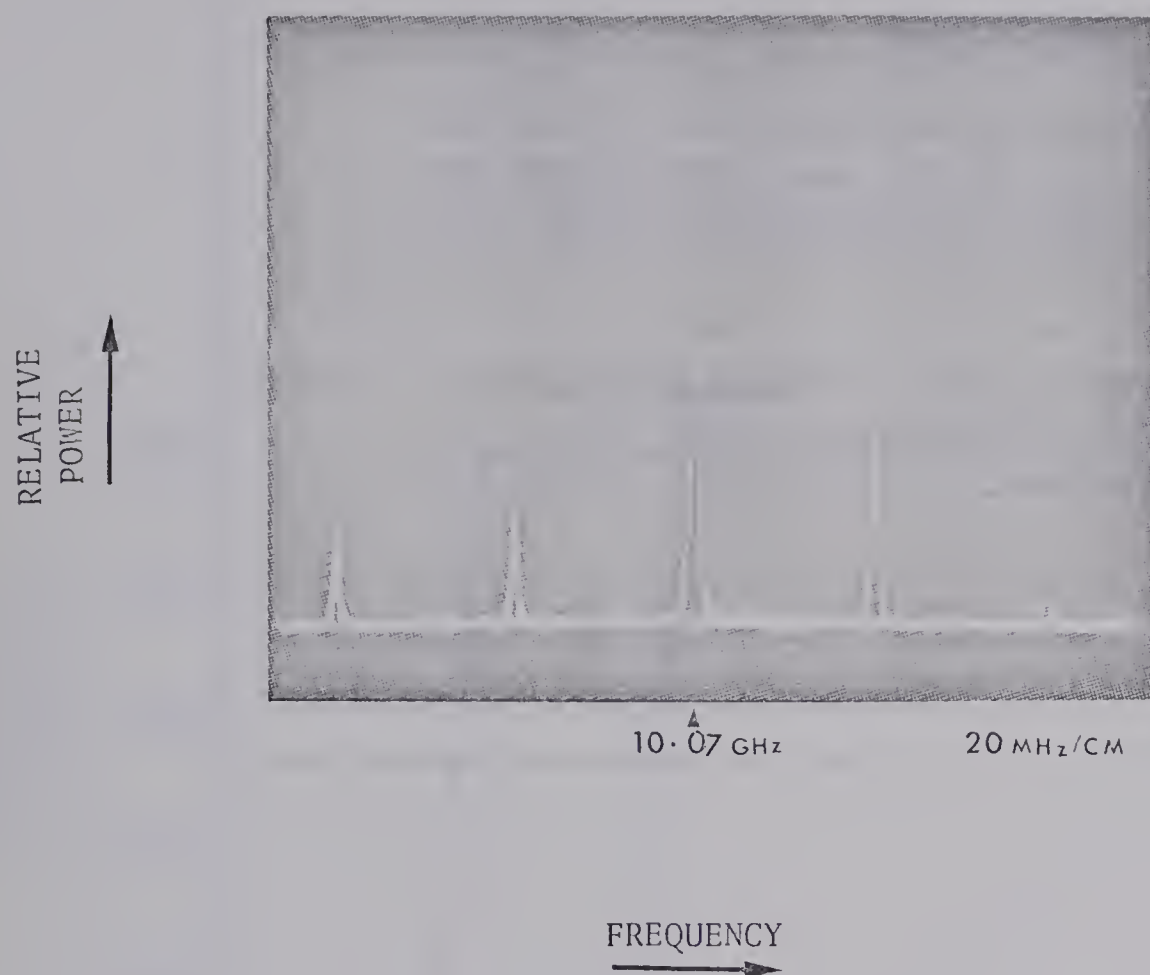


FIG. 5.9. A TYPICAL FREQUENCY SPECTRUM BEFORE A FREQUENCY JUMP.

ADO: E1128

DISTANCE OF SLIDE SCREW TUNER FROM
THE REFERENCE PLANE = $23.78 \lambda_{g0}$
SLIDE SCREW TUNER DEPTH = 0.50 cm.

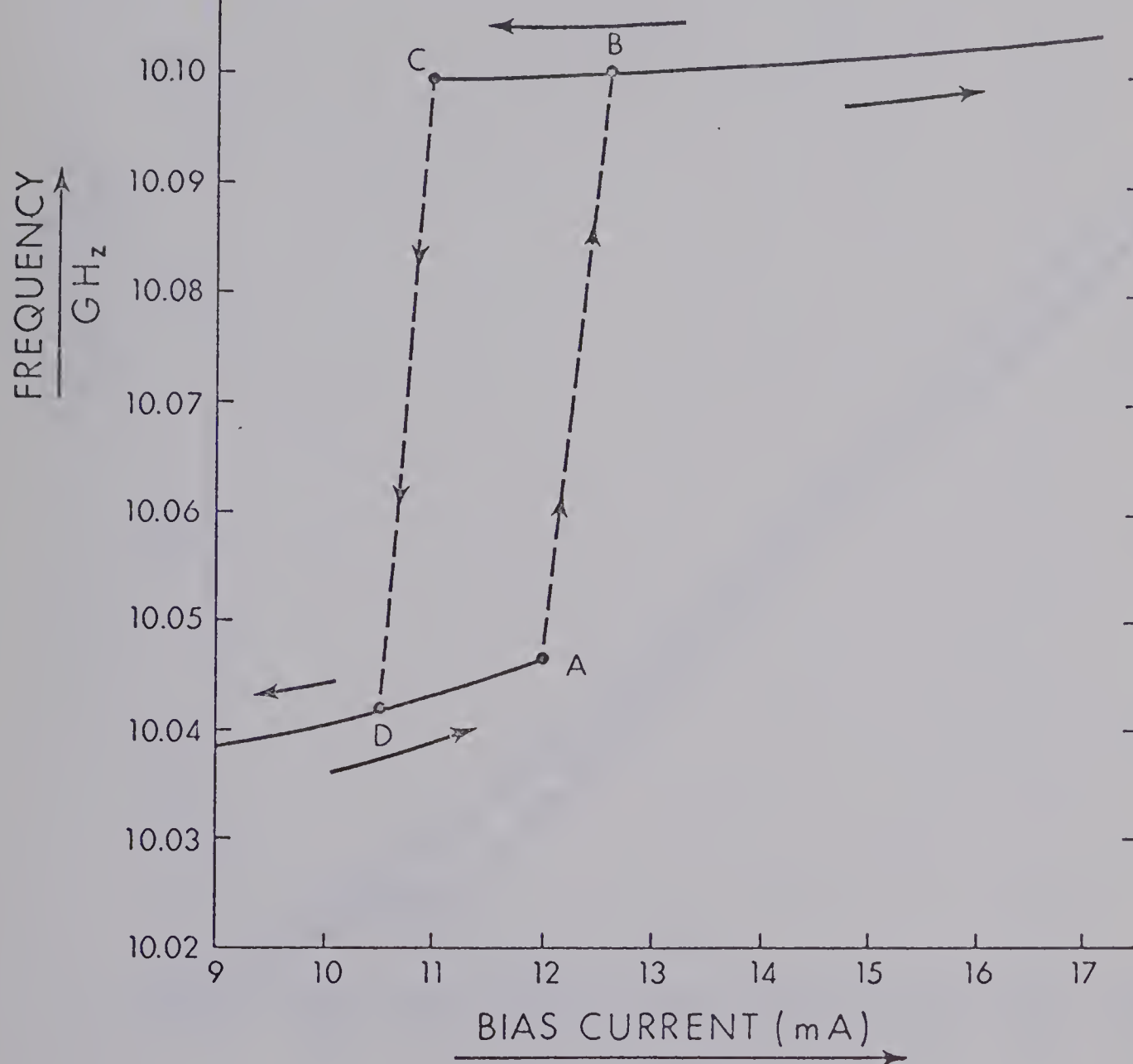


FIG. 5.10. CHANGE OF FREQUENCY WITH BIAS CURRENT
FOR A GIVEN LOAD

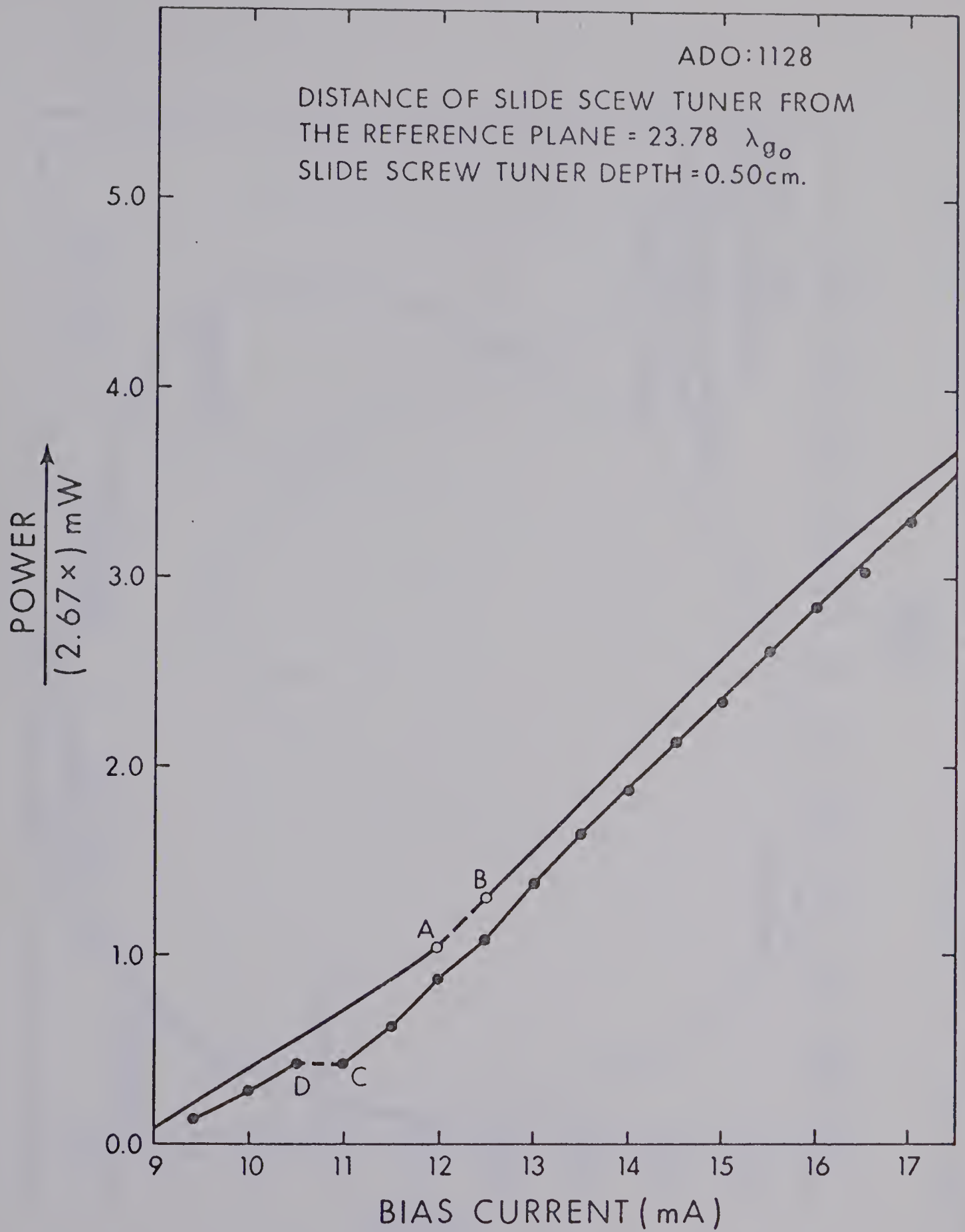


FIG. 5.11. CHANGE OF POWER WITH BIAS CURRENT
FOR A GIVEN LOAD

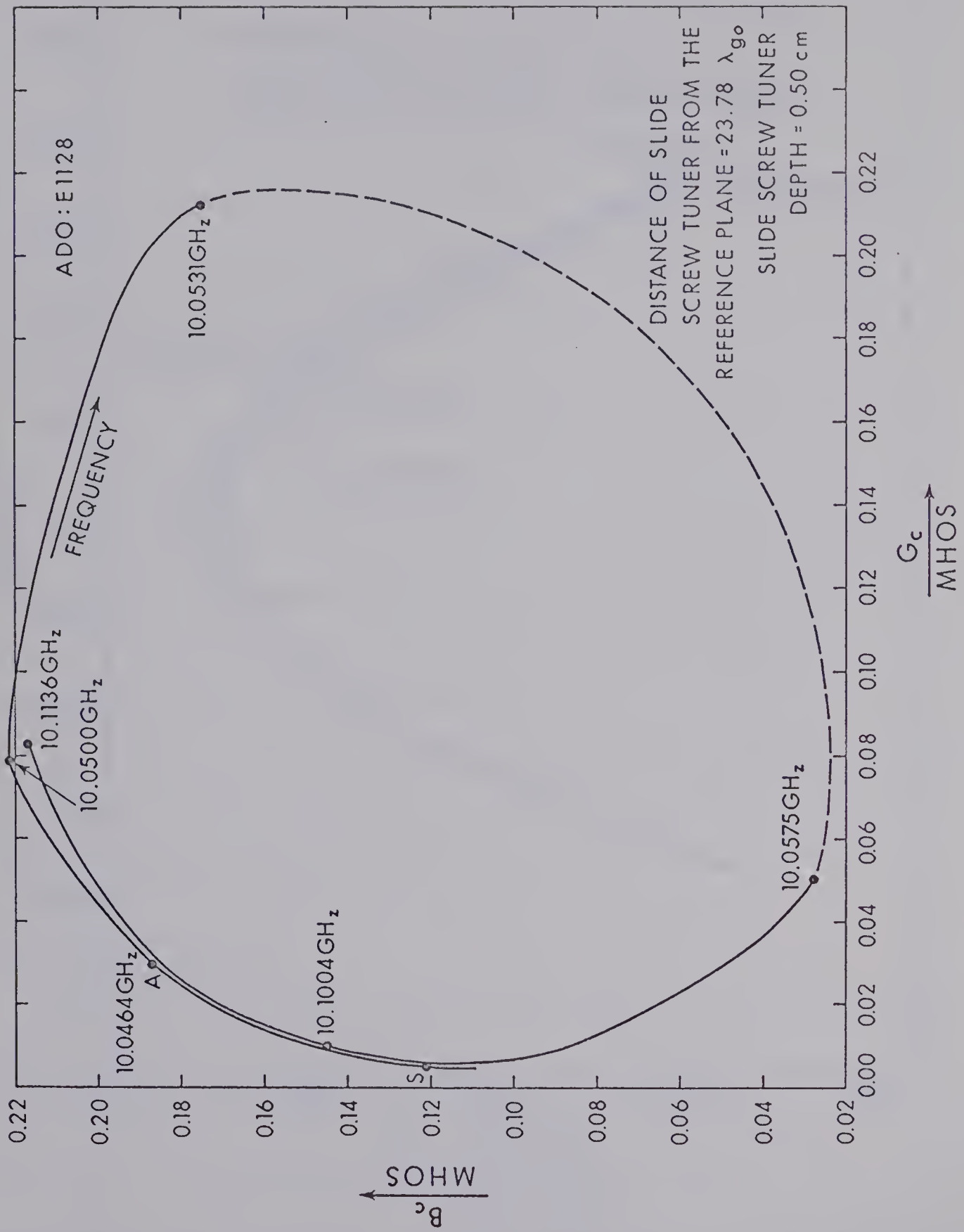


FIG. 5.12. CIRCUIT ADMITTANCE AS A FUNCTION OF FREQUENCY

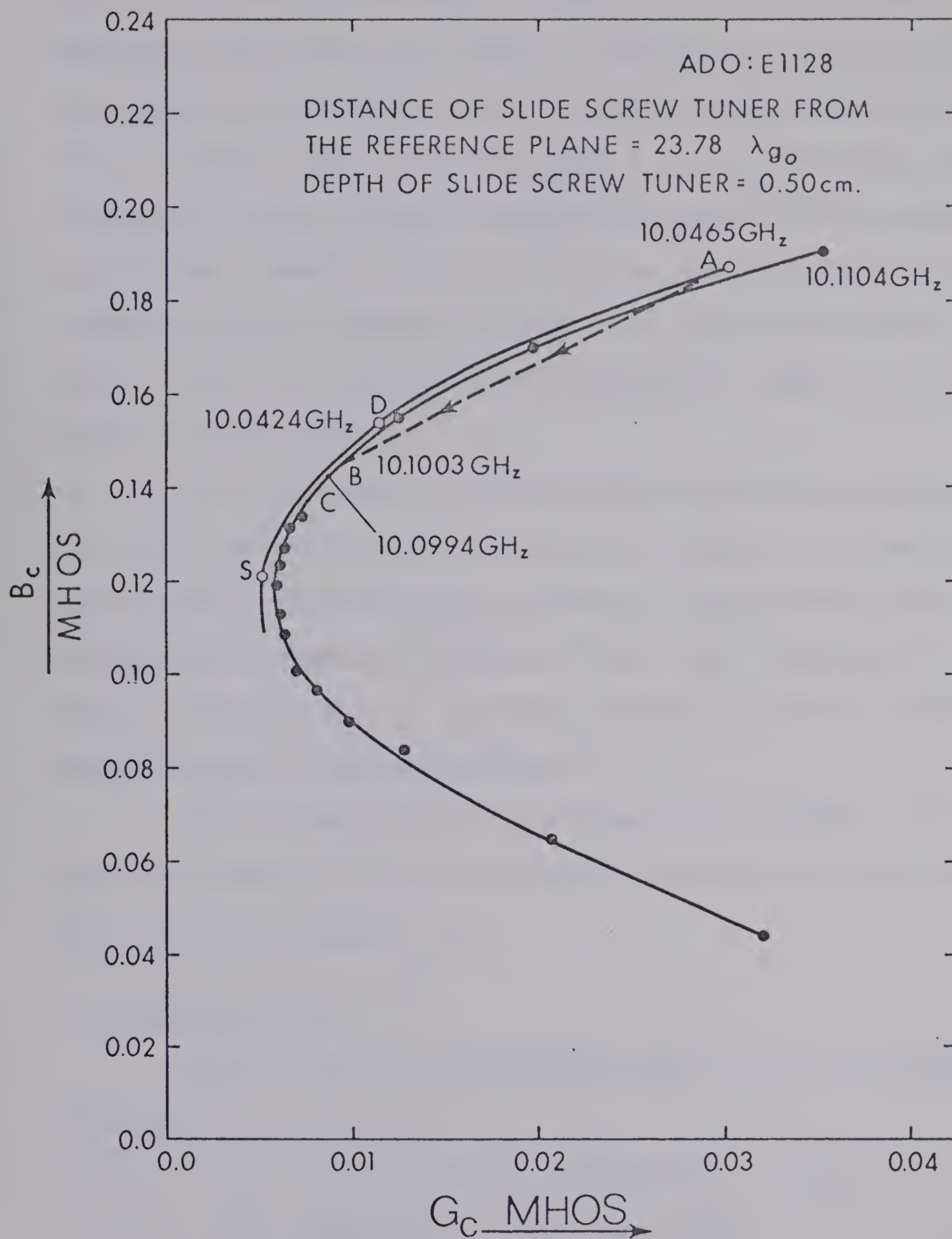


FIG. 5.13.

CHANGE OF DIODE ADMITTANCE AS A FUNCTION
OF DIODE CURRENT FOR A GIVEN LOAD

Fig. 5.10, it is seen that oscillations start at point S as expected. This is the first point at which the negative value of electronic conductance just cancels the circuit conductance G_C . As the bias current was increased, the electronic admittance followed the outer curve along S-D-A. Then the signal jumped from point A to B. With further increase in current the curve followed the inner curve from B in the increasing G_C direction. However, when the current was decreased from the maximum permissible value it reached C, beyond B and jumped tangentially to point D. Thus, the operating point of oscillation depends on the history of oscillation too.

It was experimentally observed that oscillations become very noisy when the boundary of stable region is reached. Here, parasitic oscillations at frequencies $(\omega + \Delta\omega)$ and $(\omega - \Delta\omega)$ can occur because the diode possesses negative resistance at these extra frequencies too. In contrast, when the diode is in stable operation it possesses negative resistance only at operating frequency.

Thus for satisfactory cw performance of the IMPATT oscillator, operating conditions should be such that the oscillator operates away from the unstable region.

5.7 Sources of Error

The main sources of measurement errors for the reflectometer system are:

- (1) Finite directivity of directional couplers
- (2) Adjustments in comparison set-up
- (3) Limited precision of attenuator
- (4) Limited precision of phase-shifter
- (5) Limited sensitivity of crystal detectors

(1) Finite directivity of Directional Couplers

The finite directivity of directional couplers is due to electrical and mechanical limitations, as a result of which the detector connected to the reverse coupler will contain a small signal component that is proportional to the incident wave. According to the manufacturer's specifications the directional couplers used possess a directivity better than 40dB.

(2) Adjustments in Comparison System

The main source of error is attenuation in the reflected signal sample and phase-shift in the incident signal sample, produced by the phase-shifter and attenuator respectively. Insertion loss variation of phase-shifter with phase-setting is $<0.4\text{dB}$ and phase-shift with attenuator setting is negligible. Isolators were used to prevent reflections caused by adjustments in "comparison" and "detection" systems from affecting the conditions in the main transmission line. These isolators have a minimum isolation of 30dB and maximum input reflection coefficient of 0.07. There is a maximum insertion loss of 1.0dB, but this loss is balanced out and the variation over the small frequency range of the experiment is negligible.

(3) Precision of Attenuator

The reading accuracy of the attenuator used, is better for small attenuator readings than it is for large attenuator settings (these correspond to nearly matched loads). This is because the scale of a rotary vane attenuator, which varies as $(40 \log \cos\theta)$ with angular rotation of the vane, is crowded at the higher end. Maximum error due to mechanical backlash of the (hp X382A) attenuator is less than 0.3dB. Variation of phase with attenuator setting is negligible.

(4) Precision of Phase-Shifter

The accuracy of scale reading is $\pm 2\%$ and insertion loss variation with phase-setting is $< 0.4\text{dB}$.

(5) Limited Sensitivity of the Crystal Detector

Since a certain signal-level is required before response above noise-level is obtained, it is difficult to measure nearly matched loads since the reflected power will be small. For the detectors (hp X424A) used, the low-level sensitivity is $0.4\text{mW}/\mu\text{W}$ and the micro-ammeter can read down to $0.02\mu\text{A}$.

CHAPTER VI

CONCLUSIONS

Starting with the assumption that the avalanche diode oscillator can be represented by an electronic admittance Y_e and a resonator admittance Y_r connected in parallel, these admittances were then determined experimentally.

The component values for the passive part of the equivalent circuit were evaluated by means of cold-tests. It was found that Eng's method¹³ could be employed for this purpose.

The resonant frequency of the circuit was observed to change with applied bias voltage. The variation in resonant frequency is due to change of capacitance with bias voltage. Curves of admittance of the total circuit as a function of frequency have been presented for different bias voltages, less than the breakdown voltage. From these curves, and from VSWR versus frequency plots, it is clearly seen that the behaviour is that of a double-tuned circuit, and that the Q of the diode increases as the bias voltage is increased. With increasing bias voltage, the small signal electronic admittance approaches the value of electronic admittance corresponding to cw operation. The electronic conductance G_{e1} has an appreciable positive value for small values of the bias voltages, however G_{e1} decreases with increasing bias voltage. The electronic susceptance B_{e1} gradually approaches, with increase of bias voltage, the value B_{e2} (the electronic susceptance of the diode when it is in steady-state oscillation).

The effect of external load admittance on diode behaviour was studied by plotting a Rieke diagram with the aid of a microwave reflectometer bridge. Diode operation has been observed to be very sensitive to load changes. Constant frequency curves do not coincide with constant susceptance curves on the Admittance chart; the reason for this departure from constant susceptance curves is that electronic susceptance is not independent of power.

In the Rieke diagram the constant power curves measured were not closed; however they do form a nested set. The stability conditions near the region marked "Sink" are critical. In this region, multiple frequencies can develop; in addition, frequency jumps (irregularity in frequency shift with a change of load) can occur. Thus, loads lying in this region are not suitable to obtain stable operation from an avalanche diode oscillator.

The electronic admittance Y_{e2} of the diode (admittance when in cw operation) was obtained by reduction of the load diagram. The skew nature of the constant frequency curves is caused by variation in B_{e2} with power level.

Frequency hysteresis and frequency jumps were observed both with a change of bias current and with a variation of load impedance. When the bias current (or the load impedance) was varied, such that it moved the operating point of the oscillator close to the boundary of the unstable region, extra frequency components would appear and the frequency jumped to the stronger of these parasitic components.

For further work it would be worthwhile to use the Rieke diagram for determining the suitable locking range for an avalanche diode oscillator. This should be possible because an injection-locking

signal can be thought of as being analogous to a reflection from a load. David¹⁷ showed that useful information about injection-locking, such as power-level and locking range can be obtained by drawing "constant reflection contours" on the load diagram. The regions of load diagram where frequency instability is acute and frequency jumps can occur are also regions of appreciable noise, thus these regions are not suitable for injection locking purposes.

The build-up of oscillations may be studied by a further investigation of the observed frequency jumping characteristics. After the signal frequency jumps from one value to another, by change of an oscillator parameter, the generated signal goes through a transient change in amplitude and frequency before it settles down to stable values. By a study of this transient change in signal characteristics (accompanied by a change in electronic admittance) one could obtain an "admittance compression factor". However, because of the problems associated with measurement of a quick change, the measurement technique would be quite involved and would have to be compatible with the short-time measurements of a transient.

In conclusion, the performance of an avalanche diode oscillator has been found sensitive to changes in load impedance. The electronic admittance has been determined under various operating conditions. An understanding of these phenomena will enable one to predict the manner in which the behaviour of the oscillator will be affected by changes in loading conditions.

REFERENCES

1. P. A. Goud, "Solid State Power Sources," The Journal of Microwave Power, 2 - 3, pp. 99 - 103.
2. W. T. Read, Jr., "A Proposed High-Frequency, Negative Resistance Diode," Bell Sys. Tech. J., vol. 37, pp. 401 - 446, March 1958.
3. R. L. Johnston, B. C. DeLoach, Jr., and B. G. Cohen, "A Silicon Diode Microwave Oscillator," Bell Sys. Tech. J., vol. 44, pp. 369 - 372, February 1965.
4. C. A. Lee, R. L. Batdorf, W. Wiegmann, and G. Kaminsky, "The Read Diode-An Avalanche Transit-Time, Negative Resistance Oscillator," Appl. Phys. Letters, pp. 89 - 91, March 1965.
5. M. Gilden, and M. E. Hines, "Electronic Tuning Effects in the Read Microwave Avalanche Diode," IEEE Trans. Electron Devices, vol. ED - 13, No. 1, pp. 169 - 175, January 1966.
6. H. K. Gummel, and D. L. Scharfetter, "Avalanche Region of IMPATT Diodes," Bell Sys. Tech. J., vol. 45, pp. 1797 - 1827, December 1966.
7. T. Misawa, "Negative Resistance in p-n Junctions Under Avalanche Breakdown Conditions," IEEE Trans. Electron Devices, vol. ED - 13, No. 1, pt. 1, pp. 137 - 143; pt. 2, pp. 143 - 151, January 1966.
8. K. M. Johnson, "Small-Signal Analysis of the Read Avalanche Diode," IEEE Trans. Electron Devices, vol. ED - 15, No. 3, pp. 141 - 149, March 1968.
9. W. J. Evans and G. I. Haddad, "A Large-Signal Analysis of IMPATT Diodes," IEEE Trans. Electron Devices, vol. ED - 15, No. 10, pp. 708 - 717, October, 1968.
10. D. L. Scharfetter and H. K. Gummel, "Large-Signal Analysis of a Silicon Read Diode Oscillator," IEEE Trans. Electron Devices, vol. ED - 16, No. 1, pp. 64 - 77, January 1969.
11. M. J. Ahmed, and P. A. Goud, "Electronic Admittance of Avalanche Diode Oscillators," 1969 NEREM Record, vol. 11, IEEE Catalog No. 69C43 NEREM, pp. 74 - 75, November 1969.
12. G. B. Collins, Microwave Magnetrons, M.I.T. Rad. Lab. Ser., vol. 6. New York: McGraw-Hill, 1948, pp. 330.
13. S. T. Eng, "Characterization of Microwave Variable Capacitance Diodes," IRE Trans. Microwave Theory and Techniques, pp. 11 - 22, January 1961.

14. B. C. DeLoach, "A New Microwave Measurement Technique to Characterize Diodes and an 800-Gc Cutoff Frequency Varactor at Zero Volts Bias," IEEE Trans. Microwave Theory and Techniques, pp. 15 - 20, January 1964.
15. E. L. Ginzton, Microwave Measurements. New York: McGraw-Hill, 1957.
16. M. Sucher and J. Fox, Handbook of Microwave Measurements, New York: Interscience Publishers, 1963.
17. E. E. David, Jr., "Locking Phenomenon in Microwave Oscillators," Tech. Report No. 63, Research Lab. of Electronics, MIT, April, 1948.
18. C. G. Montgomery, R. H. Dicke, and E. M. Purcell, Principles of Microwave Circuits, M.I.T. Rad. Lab. Ser., vol. 8. New York: McGraw-Hill, 1948, ch. 7.
19. J. C. Slater, Microwave Electronics. New York: D. Van Nostrand, 1963.
20. D. R. Hamilton, J. K. Knipp and J. B. H. Kuper, Klystrons and Microwave Triodes, vol. 7. New York: McGraw-Hill, 1948, pp. 414 - 435.
21. C. S. Gledhill, B. P. Walker, "Microwave Bridge Reflectometer," Proc. IEE, vol. 10, No. 10, pp. 1759 - 1763, October 1963.
22. G. E. Engen, R. W. Beatty, "Microwave Reflectometer Techniques," IRE Trans. Microwave Theory and Techniques, vol. MTT - 7, pp. 351 - 355, July 1959.
23. K. Kurokawa, "Some Basic Characteristics of Broadband Negative Resistance Oscillator Circuits," Bell Sys. Tech. J., vol. 48, pp. 1937 - 1955, July - August 1969.

APPENDIX A

ERRORS

Since most of the data were obtained experimentally they contain errors due to limited measuring accuracy, stability of the generator, personal errors, etc. To see how an error in an initial measurement propagates through subsequent calculations and affects the computation of equivalent circuit parameters, an elementary and brief numerical analysis was done.

Errors in the measurement of VSWR are due to sensitivity of the square-law detector to power and temperature variation, slot in the slotted section, and variation in the probe depth with the movement of carriage across the slotted section. The probe depth varies by an amount equal to variation in thickness of the top surface, of the slotted-section, along the line. A variation of 0.001" introduces a voltage error of 1.6% when the probe depth is 1/16". The error increases to 6.4% for a probe depth of 1/64" ¹⁶. In addition, switching scales on the VSWR indicator introduces an error of 2%.

The signal generator (hp 8690, 8694B) used for cold-tests has a stability of ± 1 MHz and the frequency meter an overall accuracy of 0.08%. The capacitance meter could contribute an error of up to (0.01pF + 0.5% of scale reading). When these errors were considered, it was found that relative error in resonator capacitance C_r and unloaded Q, Q_o of the resonator could be up to 0.04 and 0.08 respectively. Relative error in the resonant frequency of the cavity could be up to 0.001 and that in the

resonator conductance G_r up to 0.12. For the resonator inductance L_r the relative error could be as high as 0.04.

B29936